Design and operational guidelines of solar-driven catalytic conversion of CO_2 and H_2 to fuels

Sha Li, Sophia Haussener [*]

Laboratory of Renewable Energy Science and Engineering, EPFL, Station 9, Lausanne 1015, Switzerland

HIGHLIGHTS

- A steady-state model is developed for solar-driven catalytic Sabatier/RWGS processes.
- Guidelines for the design and operation of a flat transparent flow reactor are formulated.
- Reactor and system behavior in response to varying conditions is explored.
- Densely packed catalyst bed and high operating pressure lead to high performance.
- Efficiency can reach 26.3%/10.1% for Sabatier/RWGS processes at 20 kW m^{-2}.

ARTICLE INFO

ABSTRACT

Sunlight-powered catalytic conversion of CO_2 and (green) H_2 into fuels and chemicals via Sabatier and reverse water gas shift (RWGS) processes offers a promising solution to reduce greenhouse gas emissions and increase renewable energy utilization. The success of this approach relies on the development of efficient catalysts and reactors. Prior research on reactor design is based on fixed-bed concepts using conventional transition metal thermocatalysts that typically require high-temperature activation. The utilization of photothermal catalysts yields fast reaction kinetics and enhanced product selectivity at relatively low temperatures, and, therefore, requires new design and operational guidelines. A comprehensive steady-state model is described to assess the performance of solar-driven photothermal catalytic Sabatier and RWGS processes, with an emphasis on the development of a 1D heat and mass transfer model for a plate-shaped transparent flow reactor. The model allows for the prediction of the temperature profile, pressure drop and reaction extent along the reactor channel, CO_2 and H_2 conversion, total fuel yield, as well as system efficiency for a variety of design and operational choices. The effects of these parameters are strongly coupled, and a low packed bed porosity of 40% combined with high gas inlet pressure at 18–20 bar leads to both, high fuel yield and high system efficiency, for both the Sabatier and RWGS processes. The maximum system efficiency is predicted via simultaneous optimization of relevant variables within meaningful ranges while also respecting the practical temperature constraints of both the glass and catalysts. Compared with the baseline case, the optimized scenario achieves higher efficiencies of 26.3 (vs 6.7%) and 10.1% (vs 5.4%) for the Sabatier and RWGS processes, respectively, at 20 kW/m^2 irradiance. The model also identifies optimal reactor conditions under different concentrated solar irradiance, thus offering design and operational guidelines for solar-driven catalytic conversion of CO_2 and H_2 processes.

1. Introduction

Sunlight-powered catalytic conversion of CO_2 into synthetic fuels and chemicals offers great promise in closing the carbon loop and accelerating the renewable energy transition [1–3]. Among the various solar-based pathways for CO_2 reduction, a viable approach is the hydrogenation process in which CO_2 reacts with green H_2 that can be readily produced via renewable electrolysis [4]. Compared with direct CO_2 reduction requiring stringent operating conditions, CO_2 hydrogenation offers the advantage of ease of operation at moderate conditions, while also addressing the storage challenge encountered by green H_2 due to its low volumetric energy density [1]. Different products can be targeted with CO_2 hydrogenation depending on the specific catalysts

Nomenclature

a_{reac}, a_{cf}	specific surface area per volume of the packed bed channel or per volume of the cooling fluid channel (m^2)
A_{reac}	surface area of the reactor plate irradiated by concentrated sunlight (m^2)
$A_{reac,crs\text{-}sec}$	cross section area of the packed bed reactor channel (m^2)
c_p	mass specific heat capacity (J kg^{-1} K^{-1})
d_p	effective particle diameter of the catalysts in the packed bed channel (μm)
$D_{hydraulic,cf}$	hydraulic diameter of the cross section of the cooling fluid channel (m)
e	surface roughness height of the cooling fluid channel (assuming 1.5×10^{-6} m)
E_a	activation energy (kJ/mol)
f_{fric}	Darcy friction factor appearing in Eq. (20) (–)
$f_{H_2,heat}$	heat utilization factor of the FG to preheat green H_2 (–)
F_{recyc}	gas recycling fraction (–)
$f_{v,g}$	packed bed porosity or gas phase volume fraction (–)
h_{conv}	convective heat transfer coefficient (W $m^{-2}K^{-1}$)
k_0	pre-exponential factor of the Arrhenius law (s^{-1} $g_{cat}^{-1}atm^{-5n}$ or mol·s^{-1} $g_{cat}^{-1}atm^{-2}$)
k_{cond}	thermal conductivity (W $m^{-1}K^{-1}$)
k_i	specific heat ratio of species i (–)
K_1, K_2	adsorption equilibrium constant associated with CO_2 and H_2 during the RWGS process (atm^{-1})
K_{eff}	effective permeability of the catalyst packed bed (m^2)
$K_{eq,j}$	equilibrium reaction constant of chemical process j (–)
$k_{f,j}$	forward rate constant of reaction j (s^{-1} $g_{cat}^{-1}atm^{-5n}$ or mol·s^{-1} $g_{cat}^{-1}atm^{-2}$)
l	length (cm)
$L_{ch,total}$, L_{ch}	total length of all parallel channels, length of a single channel (m)
M	molar mass (kg mol^{-1})
$\dot{m}_{cf}$	mass flow rate of the cooling fluid (kg s^{-1})
n	reaction order appearing in Eq. (22) (–)
N_{ch}	number of packed bed channels that flow in parallel (–)
$\dot{n}_i$	molar flow rate of species i (mol/s)
N_{Sab}, N_{RWGS}	rate modification factor in the kinetic model of the Sabatier and RWGS processes, respectively (–)
Nu	Nusselt number (–)
Pr	Prandtl number (–)
p	pressure (bar or atm)
$q''_{solar,reac}$	concentrated solar irradiance onto the reactor (W m^{-2})
$\dot{Q}$	heat rate (W)
$r'_{chem,j}$	reaction rate of chemical process j per gram of the solid catalyst (mol g_{cat}^{-1} s^{-1})
R	universal gas constant (J/K mol^{-1})
Re	Reynolds number (–)
t	thickness (mm)
T	temperature (°C)
U	overall heat transfer coefficient (W m^{-2} K^{-1})
$v_{g,z}, v_{cf,z}$	axial velocity of the gas phase and the cooling fluid, (m/s)
w	width (mm or cm)
$\dot{W}$	work rate (W)
X_i	conversion ratio of species i (–)
$\mathbf{x}, \mathbf{y}$	column vectors appearing in Eq. (33)
y_i	molar fraction of species i in the gas phase (–)
Y_i	mass fraction of species i in the gas phase (–)

Greek symbols

α_{reac}	effective absorptivity of the catalyst packed bed (–)
ΔH	reaction enthalpy (kJ/mol)
ε_{HX_i}	heat exchanger effectiveness of HX_i (–)
ε_{reac}	effective emissivity of the catalyst packed bed (–)
η	efficiency (–)
ν_i	stoichiometric coefficient of species i associated with reaction (1) or (2) (–)
ρ	mass density (kg m^{-3})
σ	Stefan–Boltzmann constant (5.67×10^{-8} (W m^{-2} K^{-4})

Subscripts

amb	ambient condition
aux	auxiliary
btm	bottom surface/side/plate
cat	catalyst
cf	cooling fluid
ch	channel
ch-ch	inter-channel
chem	chemical reaction or process
crs-sec	cross-section
eq	thermodynamic equilibrium condition
in	reactor inlet
init	initial value
isen	isentropic process
L	lower limit
opt	optimized
out	reactor outlet
p	reactor plate, cooling fluid plate, or catalyst particle
reac	reactor
recyc	recycled gas
Sab	Sabatier reaction
sep	gas separation process
sys	system
U	upper limit

Superscripts

°	standard condition
g	gas phase
s	solid phase
T	transposed vector

Other symbol

$\langle \rangle^l, \langle \rangle$	intrinsic volume-average over phase l, superficial volume-average

Abbreviations

BC	boundary condition
CX	compressor
DNI	direct normal irradiance
GS	gas separator
LHV	lower heating value
LTE	local thermal equilibrium
HX	heat exchanger
ODE	ordinary differential equation
PO	primary optics
RWGS	reverse water gas shift
SNG	synthetic natural gas
SO	secondary optics

and the operating conditions [5]. Synthetic natural gas (SNG) serves as an attractive product given its high gravimetric energy density and its good compatibility with existing infrastructure [6]. It can be produced via the Sabatier reaction:

$$CO_2 + 4H_2 \rightarrow CH_4 + 2H_2O, \quad \Delta H_{298\ K}^{\circ} = -165.0\ kJ\ mol^{-1}. \tag{1}$$

Though the Sabatier process is highly exothermic, heat or light input is needed to initiate the reaction in order to overcome the activation energy barrier [7,8]. Carbon monoxide is another interesting chemical because it forms an important building block for the production of methanol as well as long-chain hydrocarbons [9]. It can be generated via the endothermic reverse water gas shift (RWGS) reaction:

$$CO_2 + H_2 \rightarrow CO + H_2O, \quad \Delta H_{298\ K}^{\circ} = 41.2\ kJ\ mol^{-1}. \tag{2}$$
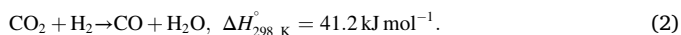
A variety of catalysts have been developed to promote the Sabatier and RWGS processes featuring different reactivity, selectivity, and stability. They can be roughly classified into thermal, photo, and photothermal types [10,11]. The conventional thermal catalysts for both processes are typically based on supported transition metals—Ru-, Rh-, Pd-, Co-, and Ni-based catalysts for the Sabatier reaction [11,12], and Pt-, Pd-, Cu-, and Pd-based catalysts for the RWGS reaction [13,14]. However, these thermal catalytic processes usually require high-temperature activation—up to 550 °C for the Sabatier process [15] and above 800 °C for the RWGS process [9]—which can lead to coke formation, particle sintering, and catalyst deactivation [13,15]. Photocatalyst options include semiconductor materials such as TiO_2 [16], g-C_3N_4 [17] and $In_2O_{3-x}(OH)_y$ [18] to harness part of the sunlight for charge carrier generation in order to drive the Sabatier or RWGS process in a photochemical way. Nevertheless, most of these photocatalysts capture only the sunlight in the UV region (around 4% of the entire solar spectrum), and, consequently, suffer from low efficiency [19]. Photothermal catalysis can exploit the combined photochemical and thermochemical contributions to drive the Sabatier or RWGS processes [20,21]. Catalysts used for this concept consist of plasmonic [22] or non-plasmonic [21] nanoparticles supported on nanostructured semiconductors or metal oxides. For example, Ru nanorods supported on γ-Al_2O_3 have been reported to promote the Sabatier reaction with 100% CH_4 selectivity and a high apparent quantum efficiency of 55% [6], while Au@TiO_2 nanocatalyst can efficiently drive the RWGS process with a CO selectivity of 98% and an apparent quantum efficiency of 4.7% [9]. Compared to thermal and photo catalysis, photothermal catalysis offers the advantages of enhanced reaction kinetics at lower temperatures and tunable absorption across the sunlight spectrum, respectively [20,21].

The performance of the solar-driven catalytic Sabatier and RWGS processes depends not only on the catalysts, but also on the reactor design that integrates the gas reactants, the solid catalyst, and the sunlight input. The gas–solid interface can be designed in many ways [15], for example packed bed [23–25] or coating [26], fluidized bed, or three-phase slurry using an inert liquid as the suspended medium [27]. The fixed bed reactor is the most widely employed concept for both the Sabatier and RWGS processes likely due to the ease of particle handling, the wide-range of operation, and the low cost of fabrication [28,29]. When it comes to the sunlight–catalyst integration, the type of the catalyst is a key design consideration. Reactors that utilize thermocatalysts can be made either transparent or opaque as long as the sunlight is converted into thermal energy via direct or indirect heating [30,31]. While those based on the photo or photothermal catalysts typically comprise a transparent quartz tube [32] or window [33,34] in order to enable direct and efficient light irradiation onto the catalysts [35]. Another factor concerning the reactor design is the endothermic or exothermic nature of the chemical reaction that is relevant for thermal management. The Sabatier reaction is strongly exothermic, so effective heat removal must be implemented in the form of active [25] or passive [28] cooling to avoid thermal runaway and reactor overheating. By

contrast, cooling is unnecessary for the endothermic RWGS process [26,36]. In addition, continuous operation and modular design with high scale-up potential are also desirable characteristics [26]. Significant research efforts have been made to develop and optimize the Sabatier and RWGS reactors based on thermo- and photo-catalysts, either in the form of monolith [37] or structured [38,39] design under continuous operation [15,35]. However, reactors that utilize the photothermal catalysts are largely limited to the monolith batch [40] or continuous [41] type using a cylindrical chamber [33,42], which is far from optimal, scalable, or industrially relevant. In addition, tubular flow reactors [43,44] are also found for photothermal catalysis with scale-up potential, but they usually require additional optics to enable uniform illumination over the tube circumference. It is thus desirable to develop a novel modular reactor for the photothermal catalytic Sabatier and RWGS processes in order to achieve continuous and efficient fuel production.

A promising solution to fulfill the above goal is the application of microflow chemistry [45,46] that has been well demonstrated in the pharmaceutical industry [47,48]. Different from the conventional batch process, the microflow chemistry offers the benefits of large surface-to-volume ratio, rapid mixing, efficient heat transfer, high product selectivity, and ease of scale-up via numbering-up strategy [45,46]. Nevertheless, this microflow technology is typically employed to promote processes in gas, liquid or slurry phases, and its application to the dry packing of solid catalyst is relatively rare [45,49]. This is likely due to the design and operational challenges to minimize the large pressure drop while also ensuring high product yield. A plate-shaped transparent packed bed flow reactor could provide a practical and scalable alternative. Mapping its performance under various design and operational choices relevant to each process will provide valuable guidelines towards efficient and fast fuel production.

We develop a process model to assess the performance of the solar-driven photothermal catalytic Sabatier and RWGS processes in order to support the design, operation, and optimization of a flat transparent packed bed flow reactor. A literature overview on Sabatier/RWGS process modelling with their corresponding performances has been added to the Supplementary Information (**SI**, see Table S1). Such a model captures the process integration at the system level and the multiphysics coupling at the reactor level. The catalysts packed within the reactor are nanoparticles of Ru@γ-Al_2O_3 [6] and Au@TiO_2 [9] for the respective Sabatier and RWGS processes that have been previously reported. Differences in reactor design and operation between the exothermic Sabatier process and the endothermic RWGS process are also highlighted.

2. Methodology

A schematic of the sunlight-powered catalytic Sabatier (Eq. (1)) or RWGS (Eq. (2)) process is shown in Fig. 1, indicating detailed mass and energy flow for pure fuel production with the system inputs being direct normal irradiance (DNI) of the terrestrial sunlight, CO_2 and green H_2. Note that the Sabatier and RWGS reactions are two independent processes aimed for different fuel products by using different catalysts and reactor cooling/operating strategies, and are therefore not proceeding simultaneously in a single reactor. The model system of the Sabatier process is composed of both, the grey and blue components, while that of the RWGS process comprises the grey components only. The additional blue components in the Sabatier process represent a cooling fluid loop that is mainly used to remove the exothermic heat release from the reactor plate for safe and efficient operation. The overall process consists of not only the Sabatier or RWGS chemical process itself, but also the up- and down- stream auxiliary components to produce pure fuel product in an efficient manner. These include the primary and secondary optics (PO and SO), gas compression, heat integration, gas recycling, and products separation and purification. Circled numbers represent different thermodynamic states during the overall process. Solar energy is assumed
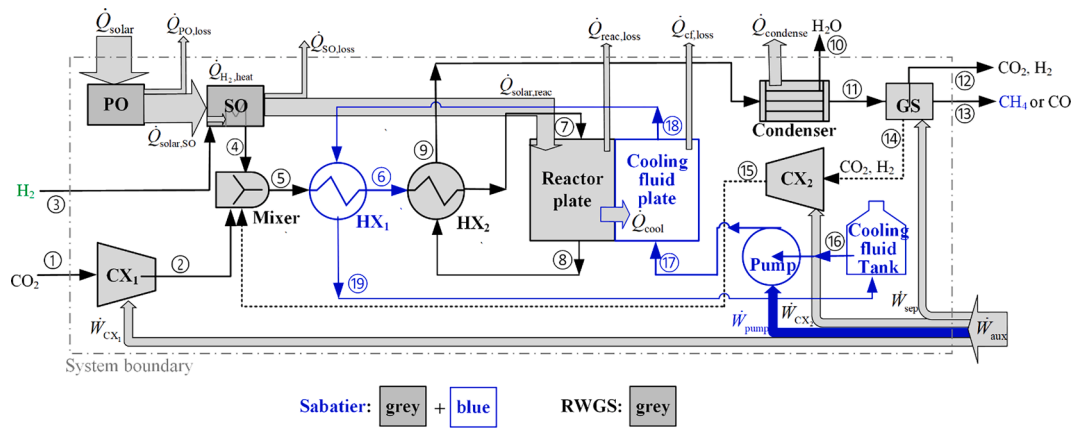
Fig. 1. Schematic of the mass and energy flow of the sunlight-powered catalytic Sabatier or RWGS process with the former consisting of both the grey and blue components while the latter consisting of the grey components only. The only inputs to the system are pure CO_2, green H_2, and DNI of the terrestrial sunlight. Circled numbers represent different thermodynamic states. Mass flow is indicated by thin arrows and energy flow by thick arrows; the energy flow arrow pointing to or from a certain component represents heat/work addition or heat removal.

the primary energy source that provides all necessary photo, thermal, and work inputs to the model system.

CO_2 captured from the point source is first pressurized by compressor CX_1 up to the reaction pressure ($1 \rightarrow 2$). Green H_2 supplied to the system (state 3) is treated to be already pressurized (usually at 30 bars) at ambient temperature assuming it is produced via solar-powered electrolysis. Because the surface reflectivity of the SO is usually imperfect (90–95%) [50], part of the concentrated sunlight is absorbed in the optics, which can be further utilized to preheat the low-temperature green H_2 ($3 \rightarrow 4$); see Eqs. (S4)–(S6) in the **SI**. The preheated H_2 is then mixed with the pressurized CO_2 ($2, 4 \rightarrow 5$). For the Sabatier process, the gas mixture will undergo two additional preheating stages in the heat exchangers HX_1 ($5 \rightarrow 6$) and HX_2 ($6 \rightarrow 7$) by the hot liquid ($18 \rightarrow 19$) and the gas products ($8 \rightarrow 9$) exiting the cooling fluid/reactor plate, respectively. In contrast, the mixed gas during the RWGS process will be preheated only in HX_2 ($5 \rightarrow 7$) by the gas products ($8 \rightarrow 9$) due to the absence of the cooling fluid loop. Finally, the gas reactants enter the Sabatier or RWGS reactor plate ($7 \rightarrow 8$) with the corresponding catalyst. The cooling fluid loop implemented exclusively for the Sabatier process is designed to flow countercurrent ($17 \rightarrow 18$) to the reactor gas stream after being pumped from the storage tank ($16 \rightarrow 17$). The product gases leaving the reactor are usually composed of multiple species (CO_2, H_2, H_2O, CH_4 or CO), and must undergo physical treatments in order to obtain pure fuel product. For example, the H_2O species can be removed using a condenser ($9 \rightarrow 10,11$) after exiting HX_2, while the unconverted CO_2 and H_2 can be extracted via a gas separator (GS) ($11 \rightarrow 12, 13, 14$). To further improve the system performance, the extracted CO_2 and H_2 can be recycled ($11 \rightarrow 14$), and then pressurized in a compressor CX_2 ($14 \rightarrow 15$) before joining the external gas supply in the mixer ($15 \rightarrow 5$). Note that the multi-component separation process in the GS may involve several steps in practical operation, and a single process is denoted in Fig. 1 for brevity.

A number of assumptions and simplifications are made: (*i*) the gas behavior follows the ideal gas law; (*ii*) the whole system is operated at steady state; (*iii*) side reactions are neglected due to the high selectivity of the catalysts (100% for the Sabatier reaction and $> 98\%$ for the RWGS reaction) [6,9]; (*iv*) the catalyst packed bed is homogeneous with uniform porosity and effective particle diameter; (*v*) local thermal equilibrium (LTE) is assumed for the two-phase gas–catalyst packed bed channel such that the gas and the solid phases share a common local temperature $\langle T_g \rangle^g = \langle T_s \rangle^s = \langle T_{reac} \rangle$; (*vi*) both, the gas flow through the packed bed channel and the liquid flow through the cooling fluid channel, are approximated as plug flow, so the gradients of concentration, velocity and temperature across each channel depth are not considered; (*vii*) the axial mass diffusion and thermal conduction within

the packed bed channel as well as the cooling fluid channel are negligible compared with other transport phenomena; (*viii*) the pressure drop across the reactor/cooling fluid plate is considered only while that pressure drop along the pipeline elsewhere is neglected; (*ix*) sunlight absorption by the catalysts is assumed wavelength-independent given their broadband absorption feature, and a wavelength-dependent treatment is left for future work; and (*x*) the catalysts are assumed to always maintain their reactivity without any degradation.

2.1. System-level model

The performance of the whole system (Fig. 1) is characterized by two metrics: the total fuel production and the system-level efficiency. The first metric is calculated assuming 100% gas recovery in the GS:

$$\dot{n}_{fuel,total} = \dot{n}_{fuel,13} = \dot{n}_{fuel,8}$$

$$= \dot{n}_{g,7} \cdot y_{CO_2,7} X_{CO_2,out} \frac{\nu_{fuel}}{\nu_{CO_2}}, \begin{cases} \text{if Sabatier, fuel } = CH_4 \\ \text{if RWGS, fuel } = CO \end{cases} \quad (3)$$

where $\dot{n}_{g,7}, y_{CO_2,7}$, $X_{CO_2,out}$ and ν_i are the gas molar flow rate and the molar fraction of CO_2 at the reactor inlet (state 7), the CO_2 conversion ratio at the reactor outlet (state 8), as well as the stoichiometric coefficient of species i in Eq. (1) or (2). The specification of $\dot{n}_{g,7}$ is closely linked to the multi-channel design of the reactor plate, as will be described in Eq. (12). The molar fraction of CO_2 is a function of the molar ratios of the feedstock species ($y_{CO_2,7} = \frac{1}{1 + \dot{n}_{H_2,ch,in}/\dot{n}_{CO_2,ch,in} + \dot{n}_{N_2,ch,in}/\dot{n}_{CO_2,ch,in}}$), which will be specified in Table 3 for each process. The determination of $X_{CO_2,out}$ relies on the condition of mass, heat, and momentum transfer as well as reaction kinetics within the packed bed reactor, making the analysis at the reactor level sufficiently important to warrant a section on its own (see **Section 2.2**). The second metric (system-level efficiency) is defined as the ratio of the chemical energy of the fuel product to the total energy inputs in the form of chemical energy, heat, and work:

$$\eta_{sys} = \frac{\dot{n}_{fuel,total} LHV_{fuel}}{\dot{n}_{H_2,3} LHV_{H_2} + \dot{Q}_{solar} + \frac{\dot{W}_{aux}}{\eta_{solar \rightarrow elec}}} \quad (4)$$

where $\dot{n}_{H_2,3}, LHV_i, \dot{Q}_{solar}$, and $\dot{W}_{aux}$ are the feeding molar flow rate of the green H_2, the lower heating value of species i, the solar thermal heat rate, and the total auxiliary work rate, respectively. The auxiliary work is primarily provided by solar energy assuming a solar to electricity conversion efficiency ($\eta_{solar \rightarrow elec}$). A similar efficiency defined using LHV values is adopted by Adelung et al. [51] to assess the performance of the

RWGS process, though efficiency based on HHV values also exists for the Sabatier process [52]. A constrained optimization scheme will be implemented in **Section 3.3** (see Eq. (33)) to maximize the system-level efficiency for both, the Sabatier and RWGS processes.

In this section, we will provide a brief overview of the model equations to reflect the determination of the performance metrics. A complete version of all governing equations is given in **section 1** of the **SI**. The solar power input appearing in Eq. (4) is determined by:

$$\dot{Q}_{solar} = \frac{1}{\eta_{optical}} A_{reac} \cdot q''_{solar,reac} \tag{5}$$

where $\eta_{optical}$, A_{reac} and $q''_{solar,reac}$ are the overall optical efficiency of the PO and SO, the reactor top surface area and the concentrated solar irradiance onto the reactor surface, respectively.

The auxiliary work input in Eq. (4) is the summation of three individual contributions:

$$\dot{W}_{aux} = \sum_{i=1}^{2} \dot{W}_{CX_i} + \dot{W}_{sep} + \dot{W}_{pump}, \tag{6}$$

where $\dot{W}_{CX_i}$, $\dot{W}_{sep}$ and $\dot{W}_{pump}$ are the work rates required for gas compression in CX_i, for gas separation in the GS, and for pumping the cooling fluid stream (Sabatier process only), respectively.

The compression work rates ($\dot{W}_{CX,1}$, $\dot{W}_{CX,2}$) can be calculated by [53]:

$$\dot{W}_{CX_i} = \frac{1}{\eta_{CX_i}} \sum_j \dot{n}_j R T_{j,l} \frac{1}{(k_j-1)} [(\frac{p_{reac,in}}{p_{j,l}})^{(k_j-1)/k_j} - 1],$$

$$\begin{cases} \text{if } i=1, & \text{then } j = CO_2, l = 1 \\ \text{if } i=2, & \text{then } j = CO_2, H_2, l = 14 \end{cases} \tag{7}$$

where $\eta_{CX_i}, \dot{n}_j, R, T_{j,l}, p_{j,l}, k_j$ are the isentropic compressor efficiency of CX_i, the flow rate of species j entering compressor i, the universal gas constant, the temperature and pressure of species j at state point l, and the specific heat ratio of species j, respectively.

The separation work rate ($\dot{W}_{sep}$) is calculated from the theoretical minimum work based on the second law of thermodynamics:

$$\dot{W}_{sep} = -\frac{1}{\eta_{sep}} R T_{sep} \cdot \sum_{i=CO_2, H_2, fuel} \left(\dot{n}_{i,11} \ln \frac{\dot{n}_{i,11}}{\sum_{i=CO_2, H_2, fuel} \dot{n}_{i,11}} \right) \tag{8}$$

where η_{sep} and T_{sep} are the separation efficiency and the separation temperature, respectively.

Finally, the pumping work rate ($\dot{W}_{pump}$) is mainly used to overcome the pressure drop across the cooling fluid channel (Δp_{cf}) that is coupled to the Sabatier reactor plate (see assumption (*viii*)):

$$\dot{W}_{pump} = \frac{1}{\eta_{pump}} \frac{\dot{m}_{cf,17}}{\rho_{cf}} \cdot \Delta p_{cf}, \begin{cases} \text{if Sabatier,} & \dot{m}_{cf} > 0 \\ \text{if RWGS ,} & \dot{m}_{cf} = 0 \end{cases} \tag{9}$$

where $\dot{m}_{cf,17}$, ρ_{cf} and η_{pump} are the mass flow rate of the cooling fluid entering the plate, the mass density of the cooling fluid, and the pump efficiency, respectively. The prediction of the Δp_{cf} depends on the analysis of the cooling fluid plate at the reactor level.

2.2. Reactor-level model

The actual design concept of the reactor component appearing in Fig. 1 is a 20 cm (l_p) × 20 cm (w_p) transparent microchannel flow reactor plate (thickness $t_{reac,p} = 2$ mm) in the presence/absence of the cooling fluid plate (thickness $t_{cf,p} = 2.25$ mm) for the Sabatier/RWGS process as illustrated in Fig. 2(a). Its inlet and outlet states are labelled using the same numbers as in Fig. 1. Both plates are made of BOROFLOAT® glass from SCOTT due to its excellent optical transmittance, high thermal shock ($\Delta T \leq 160$ °C) and chemical resistance, as well as its ability to withstand temperatures up to 450 °C for long periods. The microchannels engraved in the top plate are packed with the corresponding photothermal catalysts while those in the bottom plate are aimed to facilitate the counterflow of the cooling fluid, exclusively needed for the Sabatier process. Specifically, DW-Therm HT from Huber is selected as the cooling fluid given its wide range of operational temperature (20–340 °C). The A-A section view of the reactor/cooling fluid plate(s) is shown in Fig. 2(b). The cross-section of both the catalyst and the cooling fluid channels is in oblong shape. The depth of the catalyst channel ($t_{reac,ch}$) is set at 0.5 mm to ensure low temperature gradient [54], while that of the cooling fluid channel ($t_{cf,ch}$) is set at 1 mm to minimize the pressure drop. The channel width (w_{ch}) and the channel web distance (w_{ch-ch}) of both plates are designed as 2 mm to allow for an operating pressure of up to 20 bar. Consequently, the area coverage of the catalyst over the reactor surface is 50%, suggesting half of the irradiated sunlight will be lost via direct transmission through the glass plate without encountering the catalyst. Therefore, the total length of the packed bed channel ($L_{ch,total}$) over the reactor surface is estimated to be 10 m ($L_{ch,total} = 50\% \cdot A_{reac}/w_{ch}$). Considering the potential large pressure drop across the packed bed, the gas stream entering the reactor plate ($\dot{n}_{g,7}$) is designed to be split into N_{ch} uniform strings in parallel (Fig. 2(a)), the number of which depends on the specific design and operational conditions:

$$N_{ch} = \lceil L_{ch,total}/L_{ch} \rceil \tag{10}$$

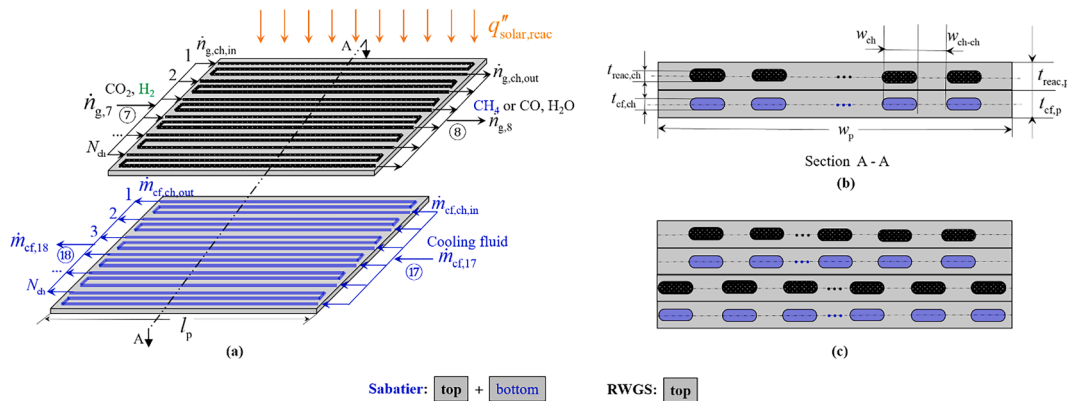where L_{ch} is the length of a single channel, and the square brackets

Fig. 2. Design specification of the plate-shaped transparent flow reactor packed with photothermal catalyst for the Sabatier or RWGS process (not to scale): (a) multi-channel design concept of the reactor component with the same boundary conditions as in Fig. 1, (b) design specification of the A-A section view, and (c) two stacked reactor plates with staggered catalyst channels to allow for efficient sunlight utilization.

denote a rounding treatment to the nearest integer. The determination of L_{ch} is subject to several practical constraints: (*i*) the outlet gas pressure should stay above 1 bar; (*ii*) the outlet reactant conversion is kept below 99% of the equilibrium value because beyond this point the gain in fuel production is marginal but the consumption in solar energy becomes unpractical; the equilibrium conversion serves as an upper limit and its determination is detailed in the **SI;** and (*iii*) the single channel length should never surpass its design limit. A mathematical expression is formulated as below:

$$\min \quad L_{ch}(\text{design choice, operational choice})$$

$$\text{subject to} \begin{cases} p_g|_{L_{ch}} \geqslant 1 \text{ bar} \\ X_i|_{L_{ch}} \leqslant 0.99 \cdot X_{i,\text{eq,out}}, \quad i = CO_2, H_2 \\ 0 < L_{ch} \leqslant L_{ch,\text{total}} \end{cases} \quad (11)$$

Consequently, the total gas flow rate entering the reactor plate is:

$$\dot{n}_{g,7} = N_{ch} \cdot \dot{n}_{g,ch,in} \quad (12)$$

where $\dot{n}_{g,ch,in}$ is the gas molar flow rate entering a single channel that will be prescribed as a boundary condition (BC) in **Section 2.2.3** (see Eq. (26)). The cooling fluid flow implemented for the Sabatier process is also configured into the same parallel pattern as the gas flow (Fig. 2(a)) to facilitate efficient heat removal:

$$\dot{m}_{cf,17} = \dot{m}_{cf,18} = N_{ch} \cdot \dot{m}_{cf,ch,in} = N_{ch} \cdot \dot{m}_{cf,ch,out} \quad (13)$$

where $\dot{m}_{cf,ch,in}$ and $\dot{m}_{cf,ch,out}$ denote the inlet and outlet mass flow rate of the cooling fluid in a single channel (see **Section 2.2.3**, see Eq. (30)). To allow for more efficient sunlight utilization, two stacked reactors can be integrated with staggered catalyst channels as shown in Fig. 2(c). However, given the complicated multiphysics occurring within a single reactor plate, the present work will focus on this concept, and investigation of the stacked concept will be left for future analysis.

2.2.1. Governing equations

A pseudo-homogeneous 1D transport model is developed for a single flow channel that is representative of the multiple (N_{ch}) ones in parallel (Fig. 2(a)). The 1D reactor model describing the coupled phenomena of mass, momentum and heat transfer as well as reaction kinetics along the axial z direction is illustrated in Fig. 3. Analysis of the Sabatier process will be performed for both the catalyst and the cooling fluid channels while that of the RWGS process will be conducted for the catalyst channel only.

Two-phase gas–catalyst packed bed channel. The generic steady-state 1D governing equations applicable to both the Sabatier and RWGS processes are based on the volume-averaging method. The mass conservation equation of the gas phase reads:

$$0 = f_{v,g} \frac{\mathrm{d}}{\mathrm{d}z} \left(\langle \rho_g \rangle^g \langle v_{g,z} \rangle^g \right) \quad (14)$$

where $f_{v,g}$, ρ_g and $v_{g,z}$ are the packed bed porosity (or gas phase volume fraction), the gas mass density and the gas velocity in the axial direction, respectively. The angle brackets with a superscript g represent intrinsic volume-averaged properties over the gas phase.

The species conservation equation accounts for bulk advection and reaction kinetics (assumption (*vii*)):

$$f_{v,g} \langle \rho_g \rangle^g \langle v_{g,z} \rangle^g \frac{\mathrm{d}}{\mathrm{d}z} \langle Y_i \rangle^g = 1000(1 - f_{v,g}) \langle \rho_s \rangle^s M_i \nu_i r'_{\text{chem},j},$$

$$\begin{cases} \text{if } j = \text{Sab}, \ i = CO_2, H_2, H_2O, CH_4 \\ \text{if } j = \text{RWGS}, \ i = CO_2, H_2, H_2O, CO \end{cases} \quad (15)$$

where $\langle Y_i \rangle^g$, M_i, $\langle \rho_s \rangle^s$ and $r'_{\text{chem},j}$ are the volume-averaged mass fraction and the molar mass of species i, the volume-averaged mass density of the solid catalyst, and the reaction rate of chemical process j per gram of the catalyst, respectively. $r'_{\text{chem,Sab}}$ and $r'_{\text{chem,RWGS}}$ are detailed in **Section 2.2.2**.

The momentum conservation equation is based on Darcy's law:

$$\frac{\mathrm{d}}{\mathrm{d}z} \left(\langle p_g \rangle^g \right) = -\frac{\mu_g}{K_{eff}} f_{v,g} \langle v_{g,z} \rangle^g \quad (16)$$

where $\langle p_g \rangle^g$, μ_g and K_{eff} are the volume-averaged pressure and the dynamic viscosity of the gas phase, as well as the effective permeability of the packed bed, respectively. The gas dynamic viscosity is calculated based on a molar-fraction weighted mixing rule, and the viscosity of each individual species is evaluated as a function of temperature [55].
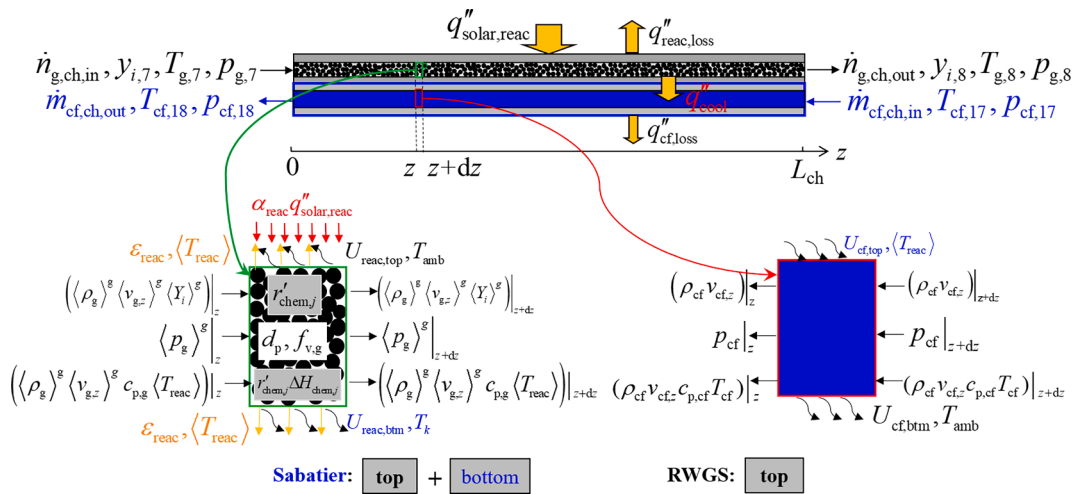

Fig. 3. Schematic of the 1D reactor model for a single flow channel that accounts for mass, momentum and heat transfer as well as reaction kinetics. Analysis of the Sabatier process is performed for both the top and bottom plates while that of the RWGS process is performed for the top plate only.

Table 1

Determination of the transport properties appearing in the governing equations of the 1D reactor model.

Parameter(s)	Function expression	Ref(s)
K_{eff}	$K_{eff} = \dfrac{f_{v,g}^3 d_p^2}{180(1 - f_{v,g})^2}$	[56]
a_{reac}, a_{cf}	$a_{reac} = \dfrac{w_{ch}}{A_{reac,crs\text{-}sec}}, a_{cf} = \dfrac{w_{ch}}{A_{cf,crs\text{-}sec}}$	–
$U_{reac,top}$	$U_{reac,top} = \dfrac{1}{\dfrac{1}{h_{conv,reac}} + \dfrac{t_{reac,top}}{k_{cond,glass}} + \dfrac{1}{h_{conv,amb}}}$ with $\dfrac{h_{conv,reac}d_p}{k_g} = Nu_{conv,reac} = 24 + 0.34Re_g^{0.77}$	[23]
$U_{reac,btm}$	$U_{reac,btm} = \dfrac{1}{\dfrac{1}{h_{conv,reac}} + \dfrac{t_{reac,btm} + t_{cf,top}}{k_{cond,glass}} + \dfrac{1}{h_{conv,cf}}}$ with $\dfrac{4h_{conv,cf}R_{cf}}{k_{cond,cf}} = Nu_{cf} = 0.027Re_{cf}^{0.8}Pr_{cf}^{1/3}$	[23]
f_{fric}	$f_{fric} = \begin{cases} \dfrac{64}{Re_{cf}}, & \text{if } Re_{cf} \leqslant 2000 \\ -\dfrac{1}{0.86\ln\left(\dfrac{e}{3.7D_{hydraulic,cf}} + \dfrac{2.51}{Re_{cf}\sqrt{f_{fric}}}\right)}, & \text{if } Re_{cf} > 2000 \end{cases}$	[57]
$U_{cf,top}$	$U_{cf,top} = \dfrac{1}{\dfrac{1}{h_{conv,cf}} + \dfrac{t_{cf,top} + t_{reac,btm}}{k_{cond,glass}} + \dfrac{1}{h_{conv,reac}}}$	[23]
$U_{cf,btm}$	$U_{cf,btm} = \dfrac{1}{\dfrac{1}{h_{conv,cf}} + \dfrac{t_{cf,btm}}{k_{cond,glass}} + \dfrac{1}{h_{conv,amb}}}$	[23]

The permeability is given in Table 1.

The energy conservation equation assuming LTE (see assumption (*v*)) reads:

$$
\begin{aligned}
f_{v,g}\langle\rho_g\rangle^g\langle v_{g,z}\rangle^g\left(\sum_{i=1}^{4}\langle Y_i\rangle^g c_{p,i}\right)\frac{\mathrm{d}\langle T_{reac}\rangle}{\mathrm{d}z} &= a_{reac}\cdot\alpha_{reac}q''_{solar,reac} \\
-(1 - f_{v,g})\langle\rho_s\rangle^s r'_{chem,j}\cdot\Delta H_{chem,j}(\langle T_{reac}\rangle) &- 2a_{reac}\varepsilon_{reac}\cdot\sigma(\langle T_{reac}\rangle^4 - T_{amb}^4) \\
-a_{reac}U_{reac,top}(\langle T_{reac}\rangle - T_{amb}) - a_{reac}U_{reac,btm}(\langle T_{reac}\rangle - T_k), &\begin{cases} \text{if } j = \text{Sab}, T_k = T_{cf} \\ \text{if } j = \text{RWGS}, T_k = T_{amb} \end{cases}
\end{aligned}
\tag{17}
$$

All terms in Eq. (17) from the left- to the right- hand sides represent the thermal convection of the bulk gas phase, the absorbed solar energy through the top surface, the heat consumption/release from chemical reaction *j*, the two-sided re-radiation heat loss by the hot catalyst, the overall conduction and convection heat losses from the top and bottom surfaces, respectively. a_{reac}, $U_{reac,top}$ and $U_{reac,btm}$ are given in Table 1 while α_{reac} and ε_{reac} will be discussed in **Section 3** (see Table 3).

Finally, the ideal gas law (see assumption (*i*)) offers a closure relationship:

$$
\langle p_g\rangle^g = \langle\rho_g\rangle^g R\langle T_{reac}\rangle\left(\sum_{i=1}^{4}\frac{\langle Y_i\rangle^g}{M_i}\right).
\tag{18}
$$

Cooling fluid channel (Sabatier only). The steady-state 1D governing equations for the single-phase cooling fluid channel are based on the orthodox continuum approach. The continuity equation reads:

$$
0 = \frac{\mathrm{d}}{\mathrm{d}z}\left(\rho_{cf}v_{cf,z}\right)
\tag{19}
$$

where ρ_{cf} and $v_{cf,z}$ are the mass density and the axial velocity of the

cooling fluid.

The 1D momentum conservation is based on the Darcy–Weisbach equation:

$$
\frac{\mathrm{d}p_{cf}}{\mathrm{d}z} = f_{fric}\frac{1}{D_{hydraulic,cf}\rho_{cf}}\frac{\left(\rho_{cf}v_{cf,z}\right)^2}{2},
\tag{20}
$$

where p_{cf}, f_{fric} and $D_{hydraulic,cf}$ are the cooling fluid pressure, the Darcy friction factor, and the hydraulic diameter of the cooling fluid channel, respectively. f_{fric} is given in Table 1.

The energy conservation equation reads:

$$
\rho_{cf}v_{cf,z}c_{p,cf}\frac{\mathrm{d}}{\mathrm{d}z}T_{cf} = -\left[a_{cf}U_{cf,top}(\langle T_{reac}\rangle - T_{cf}) - a_{cf}U_{cf,btm}(T_{cf} - T_{amb})\right]
\tag{21}
$$

where $c_{p,cf}$, a_{cf}, $U_{cf,top}$ and $U_{cf,btm}$ are the specific heat of the cooling fluid, the specific surface area of the cooling fluid channel, the overall heat transfer coefficients on the top and bottom surfaces, respectively, and the latter three terms are given in Table 1.

2.2.2. Reaction kinetics

A number of kinetic models [11] have been proposed for the Sabatier process appearing in Eqs. (15) and (17) using Ru-based catalysts. We adopt the rate law developed by Falbo et al. [58] based on the same catalyst (Ru@Al$_2$O$_3$) as in [6]:

$$
r'_{chem,Sab} = N_{Sab}k_{f,Sab}\left[\left(p_{CO_2}\right)^n\left(p_{H_2}\right)^{4n} - \frac{1}{K_{eq,Sab}^n(\langle T_{reac}\rangle)}\left(p_{CH_4}\right)^n\left(p_{H_2O}\right)^{2n}\right]
\tag{22}
$$

with the forward rate constant $k_{f,Sab}$ being expressed as:

$$
k_{f,Sab} = k_{0,Sab}\cdot\exp\left(-\frac{E_{a,Sab}}{R\langle T_{reac}\rangle}\right)
\tag{23}
$$

We introduce a dimensionless rate modification factor N_{Sab} to account for kinetic uncertainties arising from the morphology differences of the catalyst between Ref. [58] and this work, with $N_{Sab} = 1$ representing the original model [58]. Its effect will be examined in **Section 3.2**. The values of all model parameters in Eq. (22) are listed in Table 2. Note that the activation energy (~65.2 kJ mol^{-1}) in this model is similar to that (~72 kJ mol^{-1}) reported by Sastre et al. [6] based on the same photothermal catalyst Ru@Al$_2$O$_3$.

Regarding the kinetic models for the RWGS process, most are developed based on conventional thermal catalysts such as Cu or Ni [59,60]. Few models for photothermal catalyst of Au@TiO$_2$ exist but with incomplete model parameters [19]. To facilitate our analysis of the RWGS process (Eqs. (15) and (17)), the kinetic model by Kim et al. [61] based on a similar photothermal catalyst (Pt@TiO$_2$) is employed but assuming a fast desorption process:

Table 2

Specification of parameters in the kinetic models for the Sabatier and RWGS processes.

Rate model	k_0	E_a	n	K_1	K_2	Ref(s)
Eq. (22)	$9.37\,\mathrm{mol\cdot s^{-1} g_{cat}^{-1} atm^{-5n}}$	$65.2\,\mathrm{kJ\,mol^{-1}}$	0.076	–	–	[58]
Eq. (24)	$0.0947\,\mathrm{mol\cdot s^{-1} g_{cat}^{-1} atm^{-2}}$	$34.93\,\mathrm{kJ\,mol^{-1}}$	–	0.070 atm^{-1}	1.602 atm^{-1}	[19,61]

Table 3

Key parameter inputs. Values in the absence of parentheses apply to both the Sabatier and RWGS processes, otherwise those outside the parentheses are applicable to the Sabatier process while those inside the parentheses are applicable to the RWGS process.

Parameter(s)	Baseline value(s)	Parametric values	Unit
$\eta_{\mathrm{solar\rightarrow elec}}$	0.25 [62]	–	–
$\eta_{\mathrm{optical}}\cdot f_{\mathrm{H_2,heat}}$	0.75 [63], 0.6	–	–
$\eta_{\mathrm{CX}_i}, \eta_{\mathrm{pump}}$	0.85 [53], 0.70 [53]	–	–
$\varepsilon_{\mathrm{HX}_i}$	0.95 [64]	–	–
$\eta_{\mathrm{sep}}, F_{\mathrm{recyc}}$	0.1 [65], 1	–	–
$q''_{\mathrm{solar,reac}}$	5–30	–	kW m^{-2}
$\alpha_{\mathrm{reac}}, \varepsilon_{\mathrm{reac}}$	0.85, 0.85	–	–
$N_{\mathrm{Sab}} (N_{\mathrm{RWGS}})$	1 (1)	0.5–5 (0.1–10)	–
d_p	100	25–200	μm
$f_{\mathrm{v,g}}$	0.6 [66]	0.4–0.9	–
$p_{\mathrm{reac,in}}$	20 (10)	2–20	bar
$\dot{n}_{\mathrm{g,ch,in}}$	5×10^{-4}	$1\times10^{-4}–1\times10^{-3}$	mol s^{-1}
$\dot{n}_{\mathrm{H_2,ch,in}}/\dot{n}_{\mathrm{CO_2,ch,in}}$	4 (1)	1–8 (0.1–10)	–
$\dot{n}_{\mathrm{N_2,ch,in}}/\dot{n}_{\mathrm{CO_2,ch,in}}$	0 (0)	0–10 (0–5)	–
$\dot{m}_{\mathrm{cf,ch,out}}$	1×10^{-3}	$5\times10^{-4}–1\times10^{-2}$	kg s^{-1}
$p_{\mathrm{cf,18}}$	1	–	bar
$T_{\mathrm{cf,18}}$	250	200–300	°C

$$r'_{\mathrm{chem,RWGS}} = N_{\mathrm{RWGS}}\frac{k_{\mathrm{f,RWGS}}\left(p_{\mathrm{CO_2}}p_{\mathrm{H_2}} - p_{\mathrm{CO}}p_{\mathrm{H_2O}}/K_{\mathrm{eq,RWGS}}(\langle T_{\mathrm{reac}}\rangle)\right)}{\left(1 + K_{\mathrm{1,RWGS}}p_{\mathrm{CO_2}} + K_{\mathrm{2,RWGS}}p_{\mathrm{H_2}}\right)} \quad (24)$$

where $K_{\mathrm{1,RWGS}}$ and $K_{\mathrm{2,RWGS}}$ are the adsorption equilibrium constants. Again, a rate modification factor N_{RWGS} is introduced following Eq. (22) and its effect will be investigated in **Section 3.2**. To incorporate the effect of temperature, an Arrhenius type is expressed for $k_{\mathrm{f,RWGS}}$:

$$k_{\mathrm{f,RWGS}} = k_{\mathrm{0,RWGS}}\cdot\exp\left(-\frac{E_{\mathrm{a,RWGS}}}{R\langle T_{\mathrm{reac}}\rangle}\right) \quad (25)$$

where $k_{\mathrm{0,RWGS}}$ and $E_{\mathrm{a,RWGS}}$ are the respective pre-exponential factor and the activation energy. All model parameters are listed in Table 2, and the activation energy reported by Upadhye et al. [19] using the photo-thermal catalyst of Au@TiO$_2$ is adopted here.

2.2.3. Boundary conditions

The steady-state 1D coupled governing equations for the packed bed and the cooling fluid channels are in the form of first-order ordinary differential equations (ODEs), so one BC per equation is required.

Two-phase gas–catalyst packed bed channel. The BCs of the equations governing the packed bed channel (Eqs. (14)–(17)) are set at the inlet with prescribed mass flow rate, species mass fraction, pressure, and temperature:

$$\left(\langle\rho_g\rangle^g\langle v_{\mathrm{g,z,in}}\rangle^g\right)\big|_{z=0} = \frac{\dot{n}_{\mathrm{g,ch,in}}\sum_{i=1}^{2}y_{i,7}M_i}{f_{\mathrm{v,g}}A_{\mathrm{reac,crs-sec}}} \quad (26)$$

$$\langle Y_i\rangle^g\big|_{z=0} = Y_{i,7} = \frac{y_{i,7}/M_i}{\sum_{i=1}^{4}y_{i,7}/M_i} \quad (27)$$

$$\langle p_g\rangle^g\big|_{z=0} = p_{\mathrm{g,7}} = p_{\mathrm{reac,in}} \quad (28)$$

$$\langle T_{\mathrm{reac}}\rangle\big|_{z=0} = T_{\mathrm{g,7}} \quad (29)$$

where y_i is the molar fraction of species i in the gas phase. The gas pressure at the reactor inlet ($p_{\mathrm{g,7}}$) is treated to maintain the same as that ($p_{\mathrm{reac,in}}$) compressed by CX$_1$/CX$_2$.

Cooling fluid channel (Sabatier only). The BCs of the governing equations for the counterflow cooling fluid channel (see Eqs. (19)–(21)) are specified at $z = 0$ with prescribed conditions of outlet mass flow rate, pressure, and temperature:

$$\left(\rho_{\mathrm{cf}}v_{\mathrm{cf,z}}\right)\big|_{z=0} = \frac{\dot{m}_{\mathrm{cf,ch,out}}}{A_{\mathrm{cf,crs-sec}}} \quad (30)$$

$$p_{\mathrm{cf}}\big|_{z=0} = p_{\mathrm{cf,18}} \quad (31)$$

$$T_{\mathrm{cf}}\big|_{z=0} = T_{\mathrm{cf,18}} \quad (32)$$

Assigning its BCs at the same location ($z = 0$) as those of the packed bed channel facilitates the direct identification of a proper channel length (L_{ch}), subject to practical constraints under varying design and operational choices (see Eq. (11)).

2.3. Solution procedure and validation

MATLAB R2021a is used to solve the coupled, differential–algebraic equations between the reactor-level model (**Section 2.2**) and the system-level model (**Section 2.1**). The reactor-level differential equations are solved using a stiff solver (ode15s) based on variable stepsize, variable order method. While the system-level algebraic equations are solved using fminsearchbnd algorithm based on the Nelder–Mead method. Coupling between these two models relies on updating the inlet and outlet properties of the reactor/cooling fluid plate(s) by solving both models iteratively until the convergence criterion is satisfied (residuals below 10^{-5}). A flowchart describing the iterative solution is shown in Fig. 4.

Due to the lack of experimental data, validation of the reactor-level model is performed by comparing our numerical result with that predicted under thermodynamic equilibrium condition when the gas flow rate is low (thus the residence time is sufficiently long) or the reaction kinetics is fast enough. Detailed results can be found in **Fig. S2** in the **SI**.

3. Results and discussion

A summary of the key parameter inputs to the system- and reactor-level models is listed in Table 3. The baseline values of all parameters are selected to achieve a system efficiency of at least 5% for both the Sabatier and RWGS processes at the nominal 20 suns (1 sun = 1 kW m^{-2}, all direct light) condition. This is based on the apparent quantum efficiency reported in literature—4.7% for the RWGS process [9] and 55% for the Sabatier process [6]. The parametric study is performed by varying the parameters of interest within their ranges while keeping all other parameters constant at their baseline values, unless stated otherwise.

The solar-to-electricity efficiency appearing in Eq. (4) is set as 25%, a typical value that can be achieved via a dish–Stirling system or a heliostat power plant [62]. The overall optical efficiency of the PO and SO is assumed 75% based on well-established concentrating solar technologies [63]. A utilization factor of 60% of the absorbed heat by the SO (see the **SI**) is assumed to preheat H$_2$ while the remaining 40% is dissipated to the environment. The efficiency values of the compressors
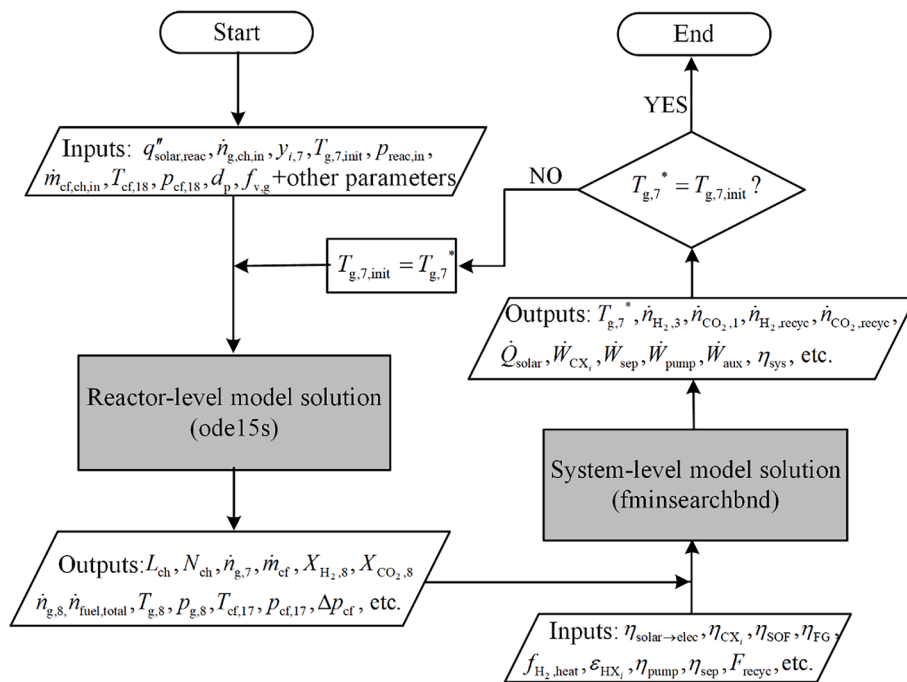
Fig. 4. Flowchart of the iterative solution procedure between the reactor and the system level models.
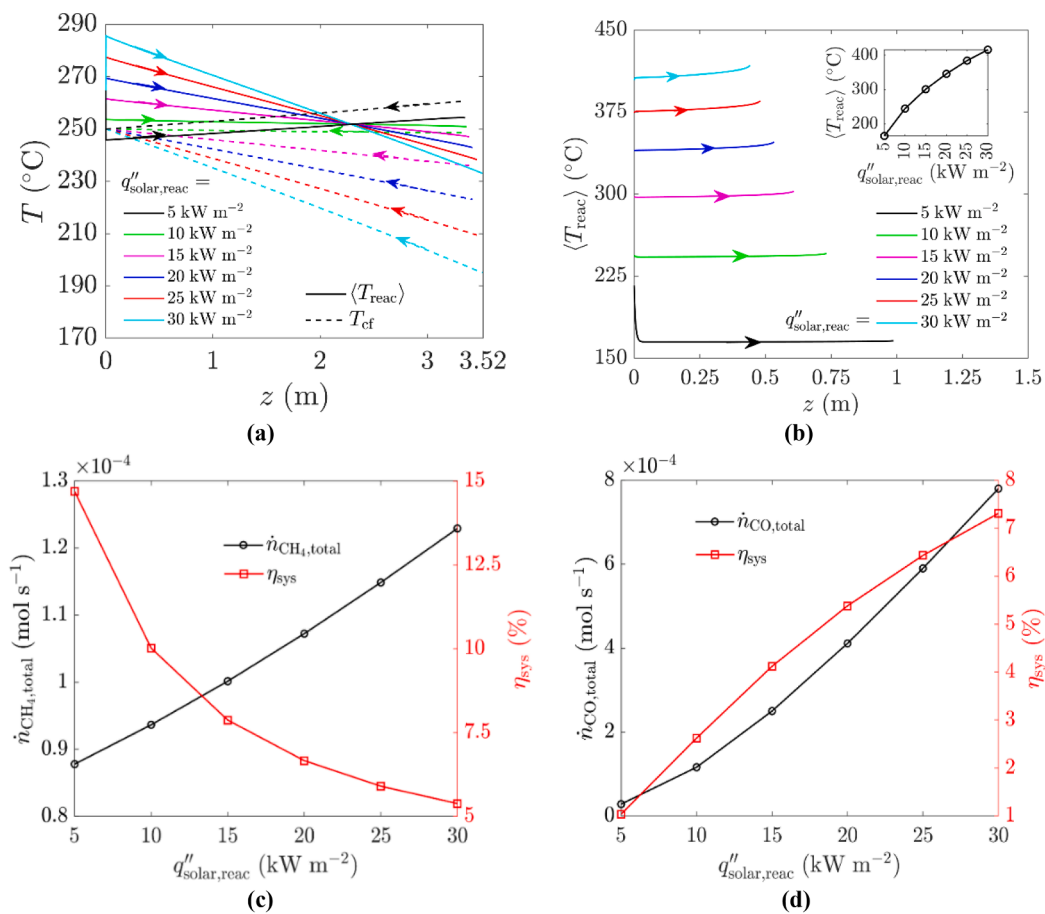

Fig. 5. Baseline performances under varying concentrated solar irradiance onto the reactor: (a) (b) axial temperature profile along a single channel with arrows indicating the flow direction, and (c) (d) total fuel production (left y-axis) and system-level efficiency (right y-axis) for the Sabatier ((a), (c)) and RWGS ((b), (d)) processes, respectively. Note that all other parameters are fixed at their baseline values as listed in Table 3.

and pump fall in the range of their typical performances [53]. The heat exchanger effectiveness is set at 0.95 given that values of over 95% have been reported [64]. A gas separation efficiency of 10% is assumed following a neutral scenario in Ref. [65], while an ideal gas recycling fraction of 100% is adopted here to aim for high system performance. The baseline concentrated solar irradiance to the reactor varies between 5 and 30 suns to account for meteorological differences in DNI that can deviate from the nominal 20 suns condition. The effective absorptivity of the catalyst packed bed (α_{reac}) in Eq. (17) is set as 85%, assuming 4% reflection loss of light from the air to the glass, 2% reflection loss from the glass to the catalyst packed bed and 9% scattering loss from the catalyst bed itself. Its effective emissivity (ε_{reac}) is assumed equals to the absorptivity according to the Kirchhoff's law. The range of the rate modification factor (N_{Sab} and N_{RWGS}) is selected to cover both slow and fast reaction kinetics while avoiding thermal runaway and large temperature gradients for the Sabatier and RWGS processes, respectively. Since the dimensions of the reactor/cooling fluid plate(s) have been specified (Section 2.2), the design space that remains flexible is the effective particle diameter d_p and the packed bed porosity $f_{v,g}$. Note that d_p differs from the actual size of the nanocatalysts due to agglomeration and clustering effects, so its range is set at the micron-scale. The baseline value of $f_{v,g}$ is 0.6, a typical value for the catalyst packed bed [66]. The maximum operating pressure within the reactor glass plate is set at 20 bar (Section 2.2). The range of the gas flow rate to a single channel is selected to yield long and short lengths for a single channel to examine which configuration performs better. Stoichiometric feeding of the reactants ($\dot{n}_{H_2,ch,in}/\dot{n}_{CO_2,ch,in}$=4 for Sabatier and = 1 for RWGS) in the absence of inert gas ($\dot{n}_{N_2,ch,in}/\dot{n}_{CO_2,ch,in}$=0) is set for the baseline scenario, and the deviation in the sub- and over-stoichiometric regimes is additionally investigated in the parametric analysis. For the cooling fluid (Sabatier only), its channel flow rates are chosen to avoid thermal runaway while also ensuring sufficient cooling, and its outlet pressure is fixed at 1 bar to allow for a minimum pump work; its outlet temperature is selected to fall within the operating window of the DW-Therm HT (see Section 2.2).

3.1. Baseline scenario

Fig. 5 depicts the baseline performances for different concentrated solar irradiance for the Sabatier and the RWGS processes. Their axial temperature profiles along a single channel are displayed in Fig. 5(a) and (b); the resulting inlet temperatures of the cooling fluid during the Sabatier process are listed in Table S2. For the Sabatier process, the concentrated solar irradiance mainly affects the temperature profile pattern. When $q''_{solar,reac}$ is extremely low (5 suns), the reaction temperature remains so low that the cooling fluid serves as a heat source rather than a sink. As the concentrated solar irradiance increases beyond 10 suns, the reaction temperature is able to surpass that of the cooling fluid. The higher the $q''_{solar,reac}$, the steeper the T_{reac} profile, favoring higher CO_2 conversion (see Fig. S3(a)). In terms of the RWGS process, a near-isothermal temperature profile is observed for all solar cases, and the stabilized temperature displays a non-linear increase with the solar irradiance (inset of Fig. 5(b)). This non-linear response is due to the fourth power law from the thermal radiation loss (see Eq. (17)); a similar trend has been reported in the experimental work by Xu et al. [54]. Consequently, higher CO_2 conversion ratio is achieved at higher irradiance (see Fig. S3(b)) due to the enhanced reaction temperature. Note that the CO_2 conversion ratios of both processes lie below the equilibrium values with the channel length being relatively short (<4m/1m for the Sabatier/RWGS process) (Fig. S3(a and b)), suggesting the slow reaction kinetics is the conversion-limiting factor. The total fuel production of each process depends not only on the outlet CO_2 conversion of a single channel, but also on the total channel number (see Eqs. (3) and (12)), and a high $X_{CO_2,out}$ combined with a short L_{ch} (thus a high N_{ch}) leads to a high total fuel yield. Both processes achieve higher total fuel

production at higher concentrated solar irradiance (Fig. 5(c) and (d)), and the fuel enhancement (at 30 suns versus 5 suns) during the RWGS process is more pronounced (20-fold for RWGS versus 41% for Sabatier). Such a big difference between these two processes is mainly due to their distinct temperature responses with respect to the solar irradiance in the presence/absence of the cooling fluid channels. Consequently, the relatively stable temperature range (200–290 °C) during the Sabatier process leads to moderate increase in CO_2 conversion (46%) but at the cost of longer channel length (5% increase, see Fig. S(a)). While the large temperature increase (from 170 °C to 400 °C) during the RWGS process contributes to the simultaneous benefits of improved CO_2 conversion (11-fold increase) and reduced channel length (55% decrease) at higher solar irradiance (see Fig. S3(b)). By contrast, the opposite trends are observed in the system efficiency for the two processes, likely due to the dominating effect of the increased solar energy input during the Sabatier process and of the enhanced fuel production during the RWGS process (see Fig. S3(c) and (d)). Given their fundamental differences in the exothermic/endothermic nature by which the Sabatier/RWGS process favors low/high temperature thus low/high solar irradiance, this is expected. The baseline efficiency under the nominal 20 suns irradiance is predicted to be 6.7% and 5.4% for the Sabatier and RWGS processes, respectively.

3.2. Parametric analysis

3.2.1. Effect of rate modification factor

The mean gas residence time in the packed bed channel usually varies from fractions of a second to a few seconds for both processes, which is short enough that the reactant conversion can be strongly affected by the reaction kinetics. Fig. 6 illustrates the effect of rate modification factor for the Sabatier (N_{Sab}) and RWGS (N_{RWGS}) processes (see Eqs. (22) and (24)) at the nominal 20 suns irradiance. Such an investigation is aimed to explore the kinetic uncertainties caused by the morphology differences in the catalysts used between the literature [58,61] and our work. Higher rate modification factors will lead to faster reaction kinetics (Eqs. (22) and (24)), which will consequently affect the heat and mass transfer (Eqs. (15) and (17)) within the packed bed channels, resulting in different temperature distribution, fuel production, and system efficiency. The axial temperature profile of each process is displayed in Fig. 6(a) and (b) with arrows indicating the flow direction. N_{Sab} is limited to 5 to prevent thermal runaway at the inlet where the temperature jumps abruptly to unrealistically high values (see Fig. S4(a)), which are highly undesirable and must be avoided in practical operation. The rate modification factor of the RWGS process is kept below 10 to ensure a temperature difference over the reactor surface of less than 50 °C (see Fig. S5(a)). For the Sabatier process, the local reaction temperature increases abruptly at the channel entrance, followed by a gradual decrease downstream the channel. The higher the N_{Sab}, the higher the temperature spike (Fig. 6(a)). This profile is a result of the counterflow configuration that simultaneously allows for fast reaction kinetics at the inlet and high reactant conversion at the outlet. For the RWGS process, the axial temperature profile shifts from a near-isothermal to a valley-like type as the rate modification factor increases from 0.5 to 10, and the higher the N_{RWGS}, the deeper the temperature drop at the inlet. The difference in the temperature profiles can be attributed to two factors:(*i*) the exothermic/endothermic nature of the reactions themselves, and (*ii*) the presence/absence of the cooling fluid channel, given the highest reaction rate always occurs at the channel inlet for both processes (see Fig. S4(b) and Fig. S5(b)).

Fig. 6(c) and (d) show the outlet CO_2 conversion ratio (left *y*-axis) along with the single channel length (right *y*-axis). Similar trends are observed for both processes: with the rate modification factor increasing, the CO_2 conversion ratio continues to increase until approaching the 99% thermodynamic equilibrium plateau (see Eq. (11)), though much higher value is predicted for the Sabatier process (0.99) than the RWGS process (0.165). Accompanying this, the channel
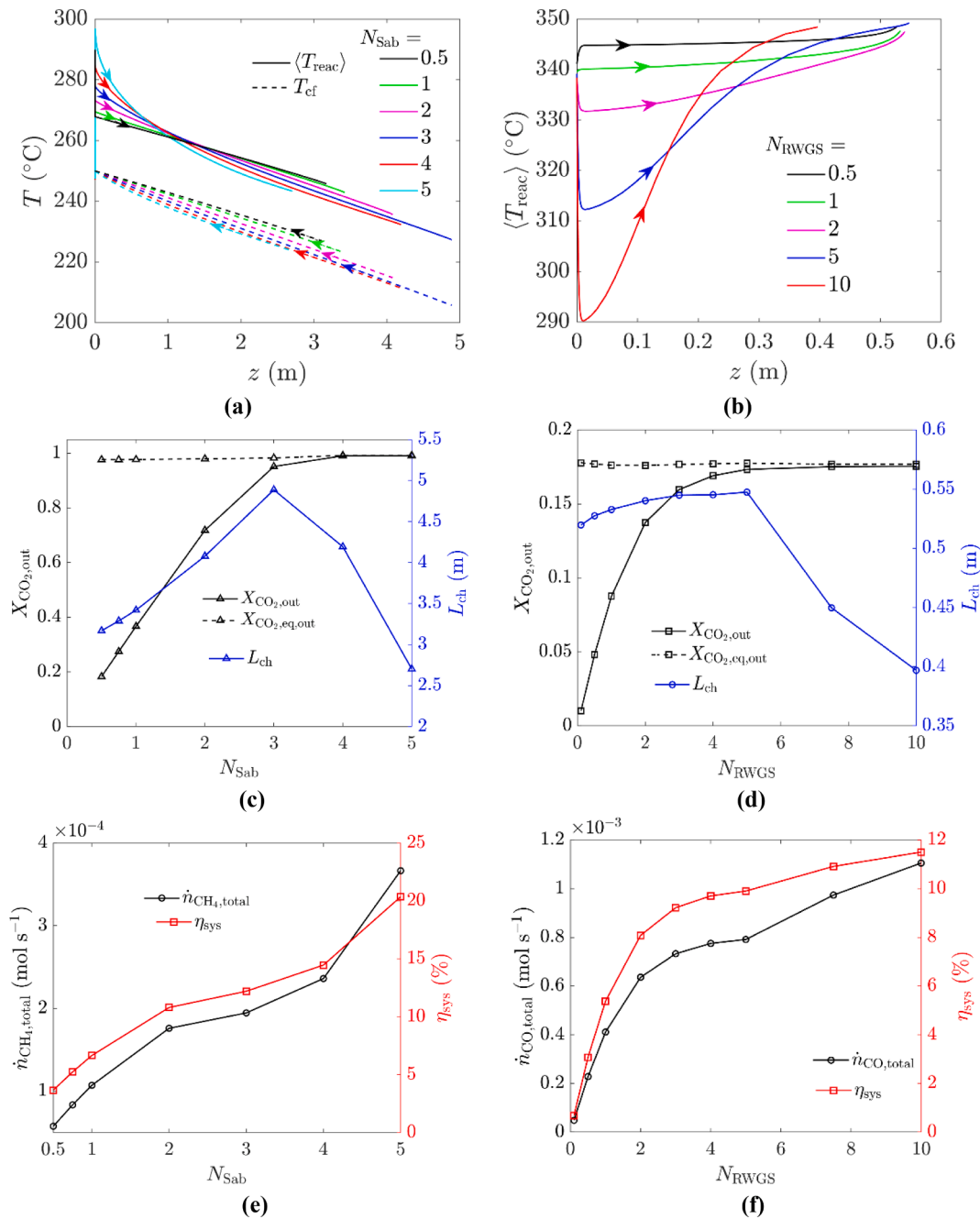
Fig. 6. Effect of rate modification factor (N_{Sab} and N_{RWGS}) on (a) (b): axial temperature profile along a single channel with arrows indicating the flow direction, on (c) (d): outlet CO_2 conversion ratio along with their corresponding equilibrium prediction (left y-axis) and length of a single channel (right y-axis), and on (e) (f): total fuel production (left y-axis) and system-level efficiency (right y-axis) for the Sabatier and RWGS processes, respectively, at 20 suns irradiance. Note that all other parameters are fixed at their baseline values as listed in Table 3.

length is found to increase first and then decrease later, whose turning point signifies a transition from a pressure-drop-limited regime to an equilibrium-limited one—a direct manifestation of Eq. (11). The axial pressure profiles at varying reaction kinetics for both processes are shown in Fig. S4(c) and Fig. S5(c). The total fuel yield (left y-axis) and the system-level efficiency (right y-axis) are illustrated in Fig. 6(e) and (f) for the Sabatier and RWGS processes. Faster reaction kinetics leads to higher fuel production and system efficiency for each process. The enhanced fuel yield at higher rate modification factor is a combined effect of the higher CO_2 conversion ratio (see Eq. (3)) and shorter channel length (thus more channels in parallel) (see Eq. (12)). While the improved efficiency is due to the dominating effect of the higher fuel yield over the higher energy consumption at faster kinetics (Fig. S4(d)

and Fig. S5(d)). However, cautious operation is advised to avoid undesirably high temperature gradient over the reactor plate if the reaction kinetics is too fast. Though the RWGS process achieves higher fuel production than the Sabatier process, its system-level efficiency turns out to be much lower (10% vs 20% at $N_{chem} = 5$). This results from the much higher penalty work arising from its lower CO_2 conversion ratio in the RWGS process than in the Sabatier process (Fig. S4(d) and Fig. S5(d)).

3.2.2. Effect of design parameters

Varying performance maps explored within the packed bed design space ($d_p, f_{v,g}$) are shown in Fig. 7 using the original kinetic model ($N_{Sab} = N_{RWGS} = 1$) for each chemical process. Fig. 7(a) and (b) depict the
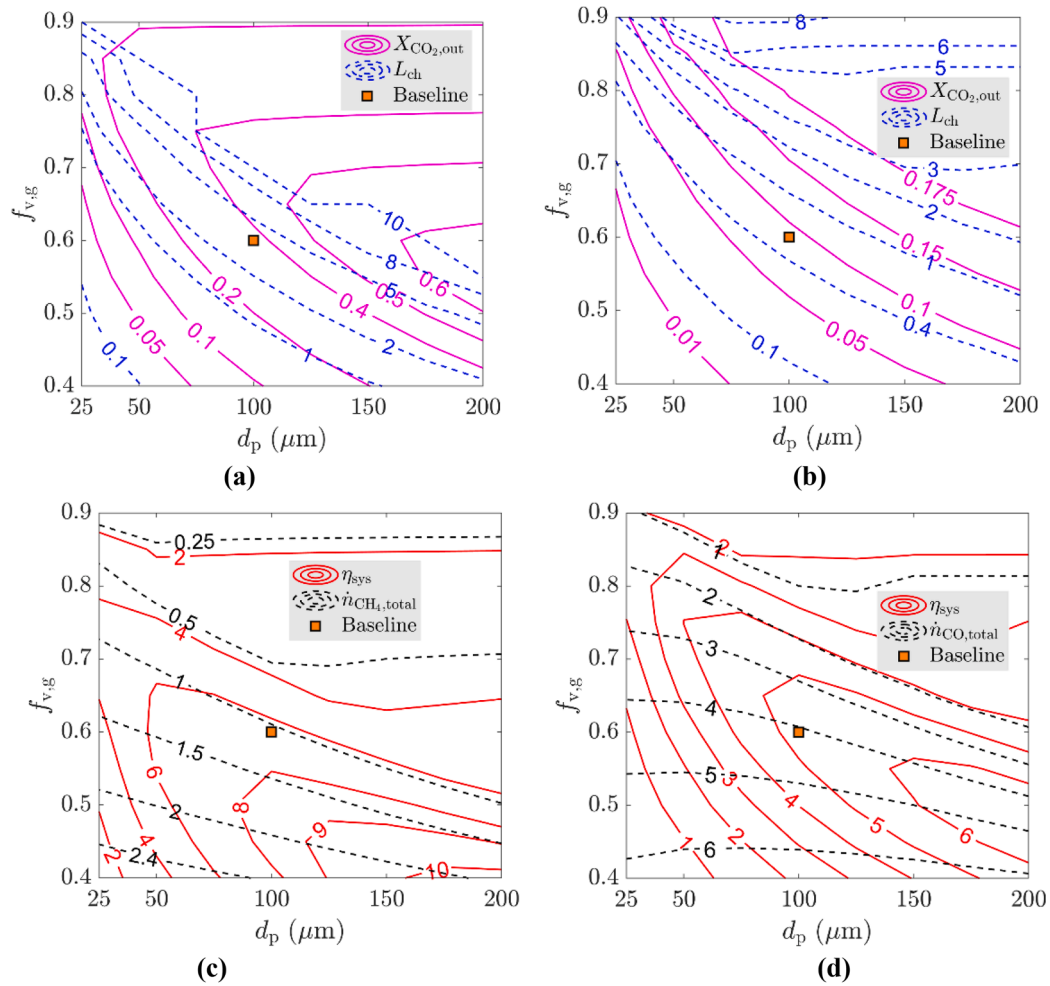
Fig. 7. Effects of the packed bed porosity and the effective particle diameter on (a) (b): outlet CO_2 conversion ratio [–] and single channel length [m], and on (c) (d): total fuel yield [10^{-4} mol/s] and system-level efficiency [%] for the Sabatier ((a), (c)) and RWGS ((b), (d)) processes, respectively, at 20 suns irradiance. The baseline results are labelled with an orange square symbol. Note that all other parameters are fixed at their baseline values as listed in Table 3.

overlay plots of the outlet CO_2 conversion ratio and the single channel length for the Sabatier and RWGS processes, respectively. Except for the region of a constant channel length maintained at 10 m in the case of the Sabatier process, a general trend is observed for both processes, i.e. a high $X_{CO_2,out}$ is accompanied by a high L_{ch}, and vice versa. This is unsurprising because a longer channel allows for longer gas residence time thus higher chemical conversion. The increased channel length and improved CO_2 conversion ratio occurring at larger d_p or higher $f_{v,g}$ are mainly due to the decreased pressure drop per unit length for both processes (see Eq. (16)). For the Sabatier process, the later drop of the $X_{CO_2,out}$ at higher $f_{v,g}$ when L_{ch} is maintained at its upper limit of 10 m

Table 4
Specification of the *x* and *y* vectors appearing in Eq. (33) for both the Sabatier and RWGS processes.

Process	x	$y = y_{opt}$	
Sabatier	$\begin{bmatrix} d_p \\ \dot{n}_{g,ch,in} \\ \dot{m}_{cf,ch,out} \end{bmatrix}$	$\begin{bmatrix} f_{v,g} \\ p_{reac,in} \\ \dot{n}_{H_2,ch,in}/\dot{n}_{CO_2,ch,in} \\ \dot{n}_{N_2,ch,in}/\dot{n}_{CO_2,ch,in} \\ T_{cf,18} \end{bmatrix} =$	$\begin{bmatrix} 0.4 \\ 20\ \text{bar} \\ 4 \\ 0 \\ 300\ °C \end{bmatrix}$
RWGS	$\begin{bmatrix} d_p \\ \dot{n}_{g,ch,in} \\ p_{reac,in} \\ \dot{n}_{H_2,ch,in}/\dot{n}_{CO_2,ch,in} \end{bmatrix}$	$\begin{bmatrix} f_{v,g} \\ \dot{n}_{N_2,ch,in}/\dot{n}_{CO_2,ch,in} \end{bmatrix} =$	$\begin{bmatrix} 0.4 \\ 0 \end{bmatrix}$

(design-limited) arises from the decreased volumetric reaction rate (see Eq. (15)). For the RWGS process, the CO_2 conversion ratio continues to increase with higher $f_{v,g}$ until approaching its equilibrium plateau (0.175), which critically constrains the channel length to below its design limit (10 m) according to Eq. (11). Consequently, the conversion limiting factor at low $f_{v,g}$ and d_p is the high pressure drop for both processes, while that at high $f_{v,g}$ and d_p shifts to the maximum channel length by design for the Sabatier process and to the thermodynamic equilibrium condition for the RWGS process.

The total fuel yield and the system-level efficiency within the design space are superimposed in Fig. 7(c) and (d) for each process. Overall, the fuel production is more sensitive to variation in $f_{v,g}$ than that in d_p, and the lower the $f_{v,g}$, the higher the fuel yield. By contrast, the system-level efficiency is highly sensitive to changes in both variables, and packed bed with low $f_{v,g}$ and high d_p contributes to high system efficiency. Since low $f_{v,g}$ favors both high fuel yield and high system efficiency, the optimal $f_{v,g}$ is selected to be fixed at its minimum value (0.4) as will be implemented in **Section 3.3** (see Table 4). On the other hand, the optimal d_p leading to the maximum fuel yield does not coincide with that resulting in the highest system-level efficiency, suggesting a design tradeoff in d_p to be made between maximizing system efficiency and total fuel yields. While the design region with the highest fuel yield can lead to quite low system efficiencies, the one with the highest system efficiency always guarantees acceptably high fuel yield (~85% of its maximum value). In addition, the highest fuel production occurs in a

scenario that represents a reactor concept with more short parallel channels (Fig. 7(a) and (b)) that is highly likely to cause oscillation in practical operation. While the scenario with the highest efficiency signifies a simple reactor design with fewer long parallel channels (Fig. 7 (a) and (b)) that would facilitate steady-state operation. Consequently, the system-level efficiency is selected as our key performance metric that will be optimized in Section 3.3 (Eq. (33)) because it allows for fast and efficient fuel production as well as ease of operation.

3.2.3. Effect of operational parameters

Unlike the packed bed design space that is limited to only two variables (d_p and $f_{v,g}$), the operational choice turns out to be quite wide, including the gas species composition, the cooling fluid conditions (Sabatier process only), the channel gas flow rate and the reactor inlet pressure. The effects of the gas species composition ($\dot{n}_{H_2,ch,in}/\dot{n}_{CO_2,ch,in}$ and $\dot{n}_{N_2,ch,in}/\dot{n}_{CO_2,ch,in}$) and the cooling fluid conditions ($\dot{m}_{cf,ch,out}$ and $T_{cf,out}$) are found to be quite intuitive and straightforward; their detailed results can be found in section 5 and 6 of the SI, and only the key findings will be summarized here. In terms of the effect of the gas species composition, stoichiometric feeding ratio of H_2 to CO_2 in the absence of N_2 leads to both the highest fuel production and system efficiency for the Sabatier process (Fig. S6), and is thus selected as its optimal condition that will be implemented in Section 3.3 (Table 4). While for the RWGS

process, the maximum fuel yield and efficiency occur at a common region where the ratio of H_2 to CO_2 deviates strongly from its stoichiometric value without the need for N_2 (Fig. S7). This is due to the much higher adsorption equilibrium constant associated with H_2 than that associated with CO_2 in Eq. (24) that would favor low H_2 partial pressure in order to achieve fast reaction rates. Consequently, the optimal ratio of N_2 to CO_2 will be fixed at 0 while that of H_2 to CO_2 will be searched via an optimization scheme as will be elaborated in Section 3.3. As to the effect of the cooling fluid conditions during the Sabatier process, both the fuel production and the system efficiency are more sensitive to the variation in $T_{cf,out}$ than that in $\dot{m}_{cf,ch,out}$, and the highest $T_{cf,out}$ results in both the maximum fuel production and efficiency (see Fig. S8). Therefore, the optimal $T_{cf,out}$ will be chosen at 300 °C while the optimal $\dot{m}_{cf,ch,out}$ will be explored in Section 3.3.

Fig. 8 illustrates the effects of the channel gas flow rate and the reactor inlet pressure on performance that display similar trends for both processes. Results of the outlet CO_2 conversion ratio and the single channel length are superimposed in Fig. 8(a) and (b) to help identify the conversion-limiting factor for the Sabatier and RWGS processes. In theory, both, the channel gas flow rate and the reactor inlet pressure, affect the gas residence time by affecting the channel length, though the former also affects the gas velocity. With the channel gas flow rate decreasing and the reactor inlet pressure increasing, both the CO_2
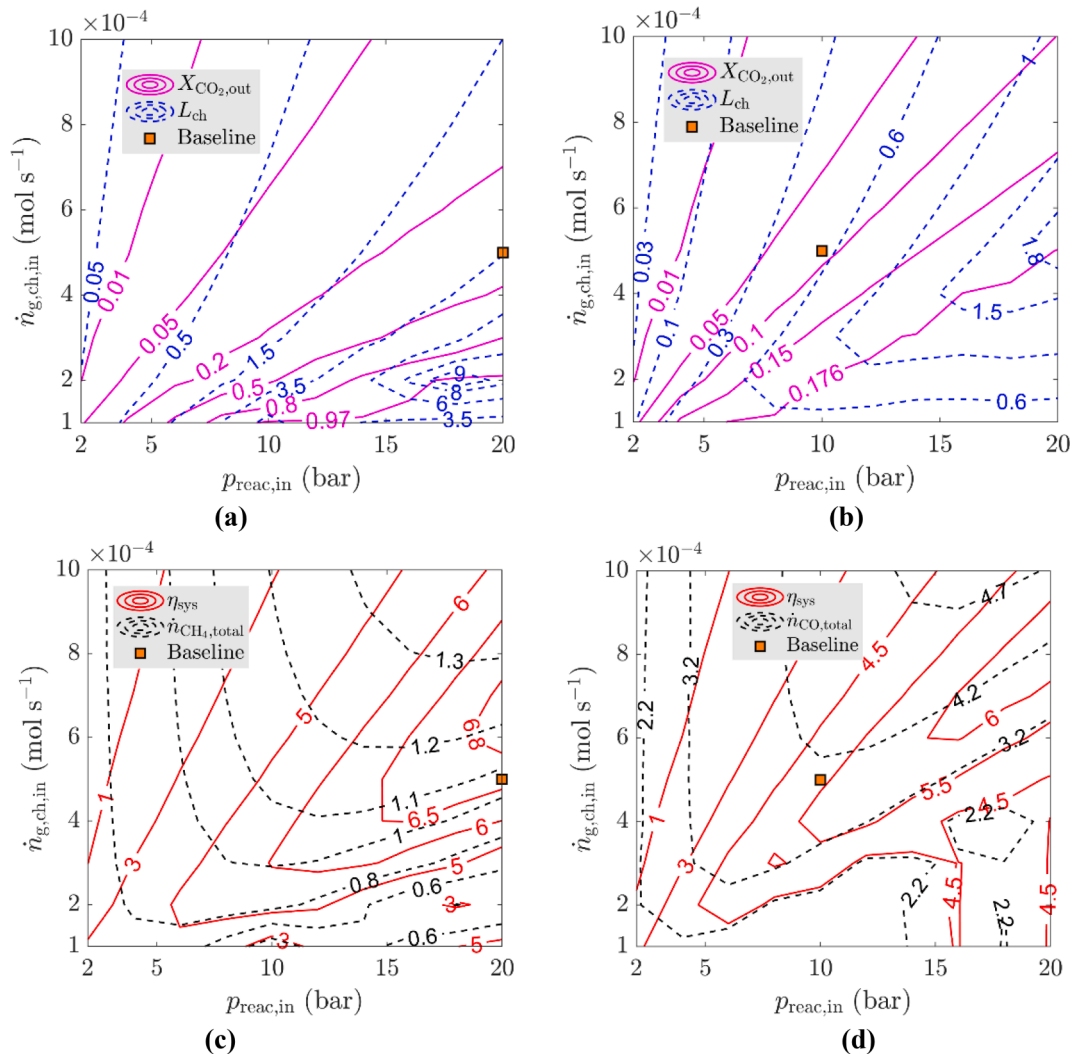

Fig. 8. Effect of the channel gas flow rate and the reactor inlet pressure on (a) (b): outlet CO_2 conversion ratio [–] and single channel length [m], and on (c) (d): total fuel production [10^{-4} mol/s] and system-level efficiency [%] for the Sabatier ((a), (c)) and RWGS ((b), (d)) processes at 20 suns irradiance. The baseline results are labelled using an orange square symbol. Note that all other parameters are fixed at their baseline values as listed in Table 3.

conversion ratio and the channel length increase until $X_{CO_2,out}$ approaches 99% of its equilibrium plateau, after which the channel length begins to decrease (see Eq. (11)). The turning point of the non-trivial trend in the channel length signifies a transition in the conversion-limiting factor that shifts from a pressure-drop limited regime at high gas flow rate and low inlet pressure to an equilibrium limited one. Fig. 8 **(c) and (d)** illustrate the overlay contour plots of the total fuel production and the system-level efficiency for each chemical process. The effects of the channel gas flow rate and the reactor inlet pressure are strongly coupled, and a high $\dot{n}_{g,ch,in}$ combined with a high $p_{reac,in}$ leads to both high fuel production and high system efficiency. The region with the highest fuel yield favors 30% (20%) higher channel gas flow rate than that with the highest efficiency for the Sabatier (RWGS) process. In addition, the highest fuel production and efficiency do not occur in the region where the CO_2 conversion ratio is maximized, suggesting high CO_2 conversion ratio does not directly translate into high fuel production and system efficiency. For the Sabatier process, since both performance metrics favor the highest reactor inlet pressure, the optimal $p_{reac,in}$ will be set at 20 bar in **Section 3.3** (see Table 4). As to the RWGS process, the optimal values of both, the $\dot{n}_{g,ch,in}$ and $p_{reac,in}$, will be searched along with other parameters via a simultaneous multi-variable optimization scheme (see Eq. (33)) in **Section 3.3**. The decision to fix the optimal $p_{reac,in}$ for the Sabatier process while leaving it variable for the RWGS process is due to the higher computational expense in the former process associated with the extra need to analyze the cooling fluid channel that would desire fewer parameters for simultaneous optimization.

3.3. Optimized scenario

The analysis conducted above has indicated strong coupling among design and operational choices. Given the relatively large number of independent variables (8 for the Sabatier process and 6 for the RWGS process), simultaneous optimization of all these parameters within their meaningful ranges (see Table 3) is challenging. To make this problem tractable, we will keep certain parameters (**y** vector) fixed at their (local) optimal values as identified in **Section 3.2** while only optimizing the remaining parameters (**x** vector) with the aim to maximize system efficiency. This is done by formulating a constrained optimization problem using the system-level efficiency as the objective function:

$$\max \quad \eta_{sys}(\boldsymbol{x}, \boldsymbol{y})$$
$$\text{subject to} \quad \begin{cases} \boldsymbol{x}_L \leqslant \boldsymbol{x} \leqslant \boldsymbol{x}_U \\ \boldsymbol{y} = \boldsymbol{y}_{opt} \\ \langle T_{reac} \rangle (\boldsymbol{x}, \boldsymbol{y}_{opt}) < 450\ °C \end{cases} \tag{33}$$

where **x** and **y** are two column vectors whose components vary with the chemical process as detailed in Table 4. Eq. (33) is solved in MATLAB using the fminsearchbnd algorithm. The temperature constraint is enforced for both processes in order to prevent catalyst deactivation and particle sintering, while also respecting the operating window of the BOROFLOAT® glass plate (see **Section 2.2**); this is particularly true for the Sabatier process that can incur destructive thermal runaway if the reaction kinetics is too fast or the solar irradiance is too high. The choice on the optimal $f_{v,g}$ and $p_{reac,in}$ for the Sabatier process is further confirmed by back-searching their optimal values that yields the same
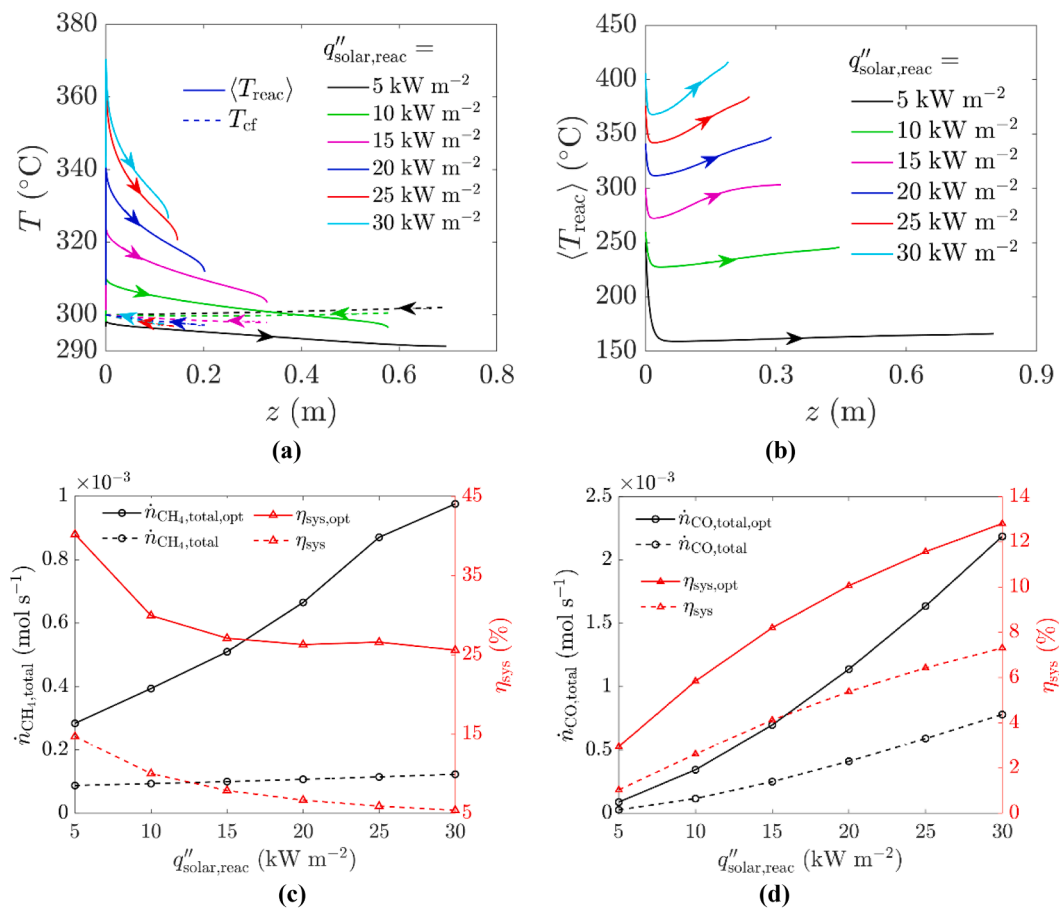

Fig. 9. Optimized results obtained via solution of optimization problem of Eq. (33) under varying concentrated solar irradiance: (a) (b) axial temperature profile along a single channel with arrows indicating the flow direction, and (c) (d) total fuel production (left *y*-axis) and system-level efficiency (right *y*-axis) for the Sabatier ((a), (c)) and RWGS ((b), (d)) processes. The baseline performances in Fig. 5**(c) and (d)** are added in Fig. 9**(c) and (d)** using dashed lines.

Table 5

Optimal **x** vectors obtained via Eq. (33) for varying concentrated solar irradiance for the Sabatier and RWGS processes (x_{opt}^T denotes the transposed vector of x_{opt}). The resulting inlet temperatures of the cooling fluid during the Sabatier process are also listed.

Process	$q''_{solar,reac}$	$x_{baseline}$	x_{opt}^T	$T_{cf,in}$
Sabatier	5 kW m^{-2}	$\begin{bmatrix} 100\,\mu m \\ 5.0 \times 10^{-4}\,mol\,s^{-1} \\ 1.0 \times 10^{-3}\,kg\,s^{-1} \end{bmatrix}$	$[189\,\mu m \quad 1.15 \times 10^{-4}\,mol\,s^{-1} \quad 1.56 \times 10^{-3}\,kg\,s^{-1}]$	302.1 °C
	10 kW m^{-2}		$[62.0\,\mu m \quad 1.51 \times 10^{-4}\,mol\,s^{-1} \quad 5.00 \times 10^{-4}\,kg\,s^{-1}]$	300.5 °C
	15 kW m^{-2}		$[43.0\,\mu m \quad 1.20 \times 10^{-4}\,mol\,s^{-1} \quad 5.01 \times 10^{-4}\,kg\,s^{-1}]$	297.9 °C
	20 kW m^{-2}		$[31.8\,\mu m \quad 1.02 \times 10^{-4}\,mol\,s^{-1} \quad 5.00 \times 10^{-4}\,kg\,s^{-1}]$	297.1 °C
	25 kW m^{-2}		$[27.5\,\mu m \quad 1.01 \times 10^{-4}\,mol\,s^{-1} \quad 5.00 \times 10^{-4}\,kg\,s^{-1}]$	296.7 °C
	30 kW m^{-2}		$[25.9\,\mu m \quad 1.00 \times 10^{-4}\,mol\,s^{-1} \quad 7.00 \times 10^{-4}\,kg\,s^{-1}]$	297.3 °C
RWGS	5 kW m^{-2}	$\begin{bmatrix} 100\,\mu m \\ 5.0 \times 10^{-4}\,mol\,s^{-1} \\ 10\,bar \\ 1.0 \end{bmatrix}$	$[151\,\mu m \quad 5.82 \times 10^{-4}\,mol\,s^{-1} \quad 17.8\,bar \quad 0.15]$	–
	10 kW m^{-2}		$[112\,\mu m \quad 5.53 \times 10^{-4}\,mol\,s^{-1} \quad 20.0\,bar \quad 0.17]$	–
	15 kW m^{-2}		$[136\,\mu m \quad 6.50 \times 10^{-4}\,mol\,s^{-1} \quad 18.2\,bar \quad 0.18]$	–
	20 kW m^{-2}		$[120\,\mu m \quad 6.12 \times 10^{-4}\,mol\,s^{-1} \quad 18.4\,bar \quad 0.19]$	–
	25 kW m^{-2}		$[112\,\mu m \quad 6.06 \times 10^{-4}\,mol\,s^{-1} \quad 18.7\,bar \quad 0.20]$	–
	30 kW m^{-2}		$[95.9\,\mu m \quad 5.60 \times 10^{-4}\,mol\,s^{-1} \quad 19.5\,bar \quad 0.21]$	–

results (0.4 and 20 bar) when keeping all other parameters fixed at their optimum obtained via Eq. (33). This is also true regarding the optimal $f_{v,g}$ (0.4) selected for the RWGS process. Note that the concentrated solar irradiance $q''_{solar,reac}$ is neither included in the **x** nor the **y** vector because it is a prescribed parameter determined by the local DNI conditions.

Fig. 9 illustrates the optimized results obtained via Eq. (33) under varying concentrated solar irradiance for both the Sabatier and RWGS processes; the baseline performances (Fig. 5(c) and (d)) are also added in Fig. 9(c) and (d) to facilitate a direct comparison. The x vector leading to these optimal efficiencies is shown in Table 5. As to the Sabatier process, unlike the baseline temperature profiles that display a linear trend (Fig. 5(a)), those in the optimized scenario (Fig. 9(a)) display a nonlinear pattern with much higher peak temperature at the channel inlet that decreases faster along the downstream region. Again, as the concentrated solar irradiance increases, the role of the cooling fluid transits from a heat source to a heat sink to maintain relatively high temperature at low solar irradiance while preventing thermal runaway at high irradiance. This change in temperature profile is a result of the enhanced inlet temperature and decreased channel flow rate of the cooling fluid and the more densely packed catalyst. With respect to the RWGS process, the temperature profile in the optimized scenario becomes more non-uniform as compared with the near-isothermal pattern in the baseline case (Fig. 5(b)), and this is more pronounced at higher concentrated solar irradiance (Fig. 9(b)). This change in temperature profile is mainly due to the sub-stoichiometric gas reactants supplied at enhanced reactor inlet pressure. Consequently, both processes achieve closer-to-equilibrium CO_2 conversion ratios within shorter parallel channels (see Fig. S9(a) and (b)), yielding more total fuel production and far higher system efficiency in the optimized scenario than those in the baseline (Fig. 9(c) and (d)). For instance, the optimal fuel output and system-level efficiency of the Sabatier process under the nominal 20 suns irradiance are 6.65×10^{-4} mol s^{-1} and 26.3%, respectively, nearly sixfold and fourfold increase compared to the corresponding baseline performances. While the optimal performances of the RWGS process under 20 suns condition are 1.14×10^{-3} mol s^{-1} and 10.1%, almost triple and double increase compared to the baseline values. The decreased efficiency during the Sabatier process at higher solar irradiance (Fig. 9(c)) results from the dominating effect of the growth in overall energy consumption (see Fig. S9(c)) over that in total fuel production. While the increased efficiency trend observed during the RWGS process (Fig. 9(d)) is due to the opposite predominance from the increased total fuel yield over the enhanced energy consumption (see Fig. S9(d)).

The optimal **x** vectors leading to Fig. 9 for both processes are listed in Table 5 along with the inlet temperatures of the cooling fluid for the Sabatier process. Except for the case of 5 suns irradiance, the Sabatier process tends to favor catalyst with smaller effective diameter and lower

channel gas flow rate as compared with the RWGS process. The optimal flow rate of the cooling fluid during the Sabatier process shifts from 5.0×10^{-4} kg s^{-1} at 10–25 suns to 7.0×10^{-4} kg s^{-1} at 30 suns in order to satisfy the temperature constraint of Eq. (33); thermal runaway is observed to occur at 30 suns irradiance when $\dot{m}_{cf,ch,out}$ stays below this optimal value (see Fig. S10). Similar to the Sabatier process, the RWGS process favors high pressures of 17.8–20 bar to facilitate high CO_2 conversion and fuel production, since a large pressure drop is anticipated for the packed bed with the lowest porosity (0.4). Unlike the optimal stoichiometric ratio (4) of H_2 to CO_2 selected for the Sabatier process, those identified for the RWGS process fall into a sub-stoichiometric range of 0.15–0.21. This is due to the adoption of the kinetic model with asymmetric adsorption equilibrium constants (Eq. (24)) that favors low H_2 partial pressure for high reaction rates. However, this trend may no longer hold if a different rate law is employed for either the Sabatier or RWGS process.

4. Conclusions

A steady-state model has been developed for the sunlight-powered catalytic Sabatier/RWGS process to aid in the design and operation of a plate-shaped transparent flow reactor. The only difference in the process configuration between the Sabatier and RWGS processes lies in the presence/absence of a cooling fluid loop that respects their exothermic/endothermic nature. This model captures the up- and downstream process integration at the system level as well as the multiphysics coupling between heat and mass transfer, fluid flow and reaction kinetics at the reactor level. Both, the reactor and system behaviors, in response to varying solar, kinetic, design and operational choices have been explored for each process.

The baseline scenario aimed to examine their performance behaviors at varying concentrated solar irradiance. As to the Sabatier process, the temperature distribution follows a linear trend, and both, the peak temperature and the profile slope, increase as the solar irradiance becomes high. Accompanied by this, the role of the cooling fluid shifts from a heat source to a sink. While for the RWGS process, near-isothermal temperature profiles are observed, and the stabilized temperature displays a sublinear increase with the solar irradiance. As a result, the Sabatier (RWGS) process achieves 41% (20-fold) higher fuel production at 30 suns irradiance than that at 5 suns condition. For the system-level efficiency, opposite trends are observed between the two reactions with increasing solar irradiance, and a baseline performance of 6.7% (5.4%) is predicted for the Sabatier (RWGS) process at 20 suns condition.

A parametric study was further carried out to understand the effects of kinetic, design and operational conditions using the nominal 20 suns irradiance as a reference case. For both the Sabatier and RWGS processes, faster kinetics simultaneously contributes to higher CO_2

conversion, fuel production as well as system efficiency. However, too fast kinetics (N_{Sab} or $N_{RWGS} > 5$) lead to high temperature gradients over the reactor surface and jeopardize safe and long-term operation. The effects of the packed bed design choices (d_p and $f_{v,g}$) are found to be strongly coupled because both parameters affect the gas residence time by influencing the pressure drop per unit length, though the porosity also affects the volumetric reaction rate. A general trend is observed for both processes, namely that a packed bed with low porosity and high effective particle diameter leads to high system efficiency as a result of the well-balanced pressure drop and enhanced volumetric reaction rate. As for the operational choices, both the channel gas flow rate and the reactor inlet pressure affect the gas residence time by influencing the channel length. Consequently, a high inlet pressure combined with a high channel gas flow rate leads to high system efficiency. However, unlike the effect of kinetics, the design/operational choice leading to the highest system efficiency does not result in the maximum CO_2 conversion or total fuel production, which are achieved at the cost of more energy consumption.

An optimized scenario was finally proposed to maximize the system efficiency by formulating a constrained optimization problem. Optimal design and operational parameters are searched within their meaningful ranges including d_p, $\dot{n}_{g,ch,in}$, and $\dot{m}_{ch,cf,out}$ (d_p, $\dot{n}_{g,ch,in}$, $p_{reac,in}$, and $\dot{n}_{H_2,ch,in}/\dot{n}_{CO_2,ch,in}$), while holding other parameters at their local optimum for the Sabatier (RWGS) process. The optimized temperature profiles of the Sabatier process become non-linear with higher peak temperatures at the channel inlet that descend faster within a shorter channel. This is mainly due to the higher inlet temperature and lower channel flow rate of the cooling fluid along with a lower packed bed porosity than those in the baseline scenario. As to the RWGS process, the temperature distribution displays a non-uniform pattern with a temperature plunge occurring at the head region followed by an increase at the tail region, all a result of the sub-stoichiometric gas feeding at higher reactor inlet pressures. Consequently, up to 6-fold/3-fold increases in fuel production and 4-fold/2-fold increases in system efficiencies are achieved for the Sabatier/RWGS process at 20 suns irradiance in the optimized scenario as compared to those in the baseline.

Although the present model is developed specifically for a plate-shaped transparent catalytic packed bed reactor, the same methodology can be applied to other reactor configurations using different catalysts. In addition, the framework described here can be readily extended to other energy conversion processes, such as thermochemical fuel production, solar energy storage, or chemical looping combustion. Overall, this work quantitatively guides the reactor design and operation towards efficient fuel production, and will ultimately contribute to the transition to a carbon–neutral society.

CRediT authorship contribution statement

Sha Li: Conceptualization, Methodology, Investigation, Writing – original draft. **Sophia Haussener:** Conceptualization, Methodology, Writing – review & editing, Supervision, Project administration, Funding acquisition.

Declaration of Competing Interest

The authors declare that they have no known competing financial interests or personal relationships that could have appeared to influence the work reported in this paper.

Data availability

Data will be made available on request.

Acknowledgements

Appendix A. Supplementary material

Supplementary data to this article can be found online at https://doi.org/10.1016/j.apenergy.2022.120617.

References

[1] Corma A, Garcia H. Photocatalytic reduction of CO_2 for fuel production: Possibilities and challenges. J Catal 2013;308:168–75.

[2] Guene Lougou B, Shuai Y, Chaffa G, Xing H, Tan H, Du H. Analysis of CO_2 utilization into synthesis gas based on solar thermochemical CH_4-reforming. J Energy Chem 2019;28:61–72.

[3] Guene Lougou B, Shuai Y, Zhang H, Ahouannou C, Zhao J, Kounouhewa BB, et al. Thermochemical CO_2 reduction over $NiFe_2O_4$@alumina filled reactor heated by high-flux solar simulator. Energy 2020;197:117267.

[4] Ye R-P, Ding J, Gong W, Argyle MD, Zhong Q, Wang Y, et al. CO_2 hydrogenation to high-value products via heterogeneous catalysis. Nat Commun 2019;10(1).

[5] Jiang X, Nie X, Guo X, Song C, Chen JG. Recent Advances in Carbon Dioxide Hydrogenation to Methanol via Heterogeneous Catalysis. Chem Rev 2020;120(15): 7984–8034.

[6] Sastre F, Versluis C, Meulendijks N, Rodríguez-Fernández J, Sweelssen J, Elen K, et al. Sunlight-Fueled, Low-Temperature Ru-Catalyzed Conversion of CO_2 and H_2 to CH_4 with a High Photon-to-Methane Efficiency. ACS Omega 2019;4(4):7369–77.

[7] Moioli E, Gallandat N, Züttel A. Parametric sensitivity in the Sabatier reaction over Ru/Al_2O_3—theoretical determination of the minimal requirements for reactor activation. React Chem Eng 2019;4(1):100–11.

[8] Moioli E, Gallandat N, Züttel A. Model based determination of the optimal reactor concept for Sabatier reaction in small-scale applications over Ru/Al_2O_3. Chem Eng J 2019;375:121954.

[9] Martínez Molina P, Meulendijks N, Xu M, Verheijen MA, Hartog T, Buskens P, et al. Low Temperature Sunlight-Powered Reduction of CO_2 to CO Using a Plasmonic Au/TiO_2 Nanocatalyst. ChemCatChem 2021;13(21):4507–13.

[10] Kho ET, Tan TH, Lovell E, Wong RJ, Scott J, Amal R. A review on photo-thermal catalytic conversion of carbon dioxide. Green Energy Environ 2017;2(3):204–17.

[11] Ashok J, Pati S, Hongmanorom P, Tianxi Z, Junmei C, Kawi S. A review of recent catalyst advances in CO_2 methanation processes. Catal Today 2020;356:471–89.

[12] Frontera P, Macario A, Ferraro M, Antonucci P. Supported Catalysts for CO_2 Methanation: A Review. Catalysts 2017;7(12):59.

[13] Su X, Yang X, Zhao B, Huang Y. Designing of highly selective and high-temperature endurable RWGS heterogeneous catalysts: recent advances and the future directions. J Energy Chem 2017;26(5):854–67.

[14] Zhu M, Ge Q, Zhu X. Catalytic Reduction of CO_2 to CO via Reverse Water Gas Shift Reaction: Recent Advances in the Design of Active and Selective Supported Metal Catalysts. Trans Tianjin Univ 2020;26(3):172–87.

[15] Rönsch S, Schneider J, Matthischke S, Schlüter M, Götz M, Lefebvre J, et al. Review on methanation—From fundamentals to current projects. Fuel 2016;166:276–96.

[16] Fang B, Xing Y, Bonakdarpour A, Zhang S, Wilkinson DP. Hierarchical $CuO–TiO_2$ Hollow Microspheres for Highly Efficient Photodriven Reduction of CO_2 to CH_4. ACS Sustain Chem Eng 2015;3(10):2381–8.

[17] Low J, Cheng B, Yu J, Jaroniec M. Carbon-based two-dimensional layered materials for photocatalytic CO_2 reduction to solar fuels. Energy Storage Mater 2016;3:24–35.

[18] He Le, Wood TE, Wu Bo, Dong Y, Hoch LB, Reyes LM, et al. Spatial Separation of Charge Carriers in $In_2O_{3-x}(OH)_y$ Nanocrystal Superstructures for Enhanced Gas-Phase Photocatalytic Activity. ACS Nano 2016;10(5):5578–86.

[19] Upadhye AA, Ro I, Zeng Xu, Kim HJ, Tejedor I, Anderson MA, et al. Plasmon-enhanced reverse water gas shift reaction over oxide supported Au catalysts. Cat Sci Technol 2015;5(5):2590–601.

[20] Mateo D, Cerrillo JL, Durini S, Gascon J. Fundamentals and applications of photo-thermal catalysis. Chem Soc Rev 2021;50(3):2173–210.

[21] Ghoussoub M, Xia M, Duchesne PN, Segal D, Ozin G. Principles of photothermal gas-phase heterogeneous CO_2 catalysis. Energ Environ Sci 2019;12(4):1122–42.

[22] Luo S, Ren X, Lin H, Song H, Ye J. Plasmonic photothermal catalysis for solar-to-fuel conversion: current status and prospects. Chem Sci 2021;12(16):5701–19.

[23] Sun D, Simakov DSA. Thermal management of a Sabatier reactor for CO_2 conversion into CH_4: Simulation-based analysis. J CO2 Util 2017;21:368–82.

[24] Zhang L, Chen L, Xia S, Wang C, Sun F. Entropy Generation Minimization for Reverse Water Gas Shift (RWGS) Reactors. Entropy (Basel) 2018;20(6):415.

[25] Gruber M, Wiedmann D, Haas M, Harth S, Loukou A, Trimis D. Insights into the catalytic CO_2 methanation of a boiling water cooled fixed-bed reactor: Simulation-based analysis. Chem Eng J 2021;406:126788.

[26] Cao XE, Kaminer Y, Hong T, Schein P, Liu T, Hanrath T, et al. HI-Light: A Glass-Waveguide-Based "Shell-and-Tube" Photothermal Reactor Platform for Converting CO_2 to Fuels. iScience 2020;23(12):101856.

[27] Ola O, Maroto-Valer M, Liu D, Mackintosh S, Lee C-W, Wu JCS. Performance comparison of CO_2 conversion in slurry and monolith photoreactors using Pd and

Rh-TiO$_2$ catalyst under ultraviolet irradiation. Appl Catal B: Environ 2012;126: 172–9.

[28] Alarcón A, Guilera J, Andreu T. An insight into the heat-management for the CO$_2$ methanation based on free convection. Fuel Process Technol 2021;213:106666.

[29] Ghodoosi F, Khosravi-Nikou MR, Shariati A. Mathematical Modeling of Reverse Water-Gas Shift Reaction in a Fixed-Bed Reactor. Chem Eng Technol 2017;40(3): 598–607.

[30] Zhang W, Machida H, Takano H, Izumiya K, Norinaga K. Computational fluid dynamics simulation of CO$_2$ methanation in a shell-and-tube reactor with multi-region conjugate heat transfer. Chem Eng Sci 2020;211:115276.

[31] Wolf A, Jess A, Kern C. Syngas Production via Reverse Water-Gas Shift Reaction over a Ni-Al$_2$O$_3$ Catalyst: Catalyst Stability, Reaction Kinetics, and Modeling. Chem Eng Technol 2016;39(6):1040–8.

[32] Albero J, Dominguez E, Corma A, García H. Continuous flow photoassisted CO$_2$ methanation. Sustainable Energy Fuels 2017;1(6):1303–7.

[33] Rohlfs J, Bossers KW, Meulendijks N, Valega Mackenzie F, Xu M, Verheijen MA, et al. Continuous-Flow Sunlight-Powered CO$_2$ Methanation Catalyzed by γ-Al$_2$O$_3$-Supported Plasmonic Ru Nanorods. Catalysts 2022;12(2):126.

[34] Ren J, Ouyang S, Xu H, Meng X, Wang T, Wang D, et al. Targeting Activation of CO$_2$ and H$_2$ over Ru-Loaded Ultrathin Layered Double Hydroxides to Achieve Efficient Photothermal CO$_2$ Methanation in Flow-Type System. Adv Energy Mater 2017;7(5):1601657.

[35] Nguyen V-H, Wu JCS. Recent developments in the design of photoreactors for solar energy conversion from water splitting and CO$_2$ reduction. Appl Catal A: General 2018;550:122–41.

[36] Wenzel M, Rihko-Struckmann L, Sundmacher K. Thermodynamic analysis and optimization of RWGS processes for solar syngas production from CO$_2$. AIChE J 2017;63(1):15–22.

[37] Schlereth D, Hinrichsen O. A fixed-bed reactor modeling study on the methanation of CO$_2$. Chem Eng Res Des 2014;92(4):702–12.

[38] Brooks KP, Hu J, Zhu H, Kee RJ. Methanation of carbon dioxide by hydrogen reduction using the Sabatier process in microchannel reactors. Chem Eng Sci 2007; 62(4):1161–70.

[39] Stiegler T, Meltzer K, Tremel A, Baldauf M, Wasserscheid P, Albert J. Development of a Structured Reactor System for CO$_2$ Methanation under Dynamic Operating Conditions. Energ Technol 2019;7(6):1900047.

[40] Steeves TM, Esser-Kahn AP. Demonstration of the photothermal catalysis of the Sabatier reaction using nickel nanoparticles and solar spectrum light. RSC Adv 2021;11(14):8394–7.

[41] Meng X, Wang T, Liu L, Ouyang S, Li P, Hu H, et al. Photothermal conversion of CO$_2$ into CH$_4$ with H$_2$ over Group VIII nanocatalysts: an alternative approach for solar fuel production. Angew Chem Int Ed Engl 2014;53(43):11478–82.

[42] Wu Z, Li C, Li Z, Feng K, Cai M, Zhang D, et al. Niobium and Titanium Carbides (MXenes) as Superior Photothermal Supports for CO$_2$ Photocatalysis. ACS Nano 2021;15(3):5696–705.

[43] Li Y, Bai X, Yuan D, Zhang F, Li Bo, San X, et al. General heterostructure strategy of photothermal materials for scalable solar-heating hydrogen production without the consumption of artificial energy. Nat Commun 2022;13(1).

[44] Sun J, Sun W, Wang Lu, Ozin GA. Uniting Heat and Light in Heterogeneous CO$_2$ Photocatalysis: Optochemical Materials and Reactor Engineering. Accounts Mater Res 2022;3(12):1260–71.

[45] Oelgemoller M, Shvydkiv O. Recent advances in microflow photochemistry. Molecules 2011;16(9):7522–75250.

[46] Noël T. Micro flow chemistry: new possibilities for synthetic chemists. Discovering Future Mol Sci 2014:137–64.

[47] Hughes DL. Applications of Flow Chemistry in Drug Development: Highlights of Recent Patent Literature. Org Process Res Dev 2018;22(1):13–20.

[48] Bogdan AR, Dombrowski AW. Emerging Trends in Flow Chemistry and Applications to the Pharmaceutical Industry. J Med Chem 2019;62(14):6422–68.

[49] Sambiagio C, Noël T. Flow Photochemistry: Shine Some Light on Those Tubes! Trends Chem 2020;2(2):92–106.

[50] Meller Y, Kribus A. Kaleidoscope homogenizers sensitivity to shading. Sol Energy 2013;88:204–14.

[51] Adelung S, Maier S, Dietrich R-U. Impact of the reverse water-gas shift operating conditions on the Power-to-Liquid process efficiency. Sustain Energy Technol Assess 2021;43:100897.

[52] Jürgensen L, Ehimen EA, Born J, Holm-Nielsen JB. Dynamic biogas upgrading based on the Sabatier process: thermodynamic and dynamic process simulation. Bioresour Technol 2015;178:323–9.

[53] Moran MJ, Shapiro HN, Boettner DD, Bailey MB. Fundamentals of engineering thermodynamics. John Wiley & Sons; 2010.

[54] Xu M, Hartog T, Cheng L, Wolfs M, Habets R, Rohlfs J, et al. Using Fiber Bragg Grating Sensors to Quantify Temperature Non-Uniformities in Plasmonic Catalyst Beds under Illumination. ChemPhotoChem 2022;6(4).

[55] Yaws CL. Transport properties of chemicals and hydrocarbons. William Andrew; 2014.

[56] Kaviany M. Principles of Heat Transfer in Porous Media. Springer Science & Business Media; 2012.

[57] Potter MC, Wiggert DC, Ramadan BH. Mechanics of fluids. Cengage learning 2016.

[58] Falbo L, Martinelli M, Visconti CG, Lietti L, Bassano C, Deiana P. Kinetics of CO$_2$ methanation on a Ru-based catalyst at process conditions relevant for Power-to-Gas applications. Appl Catal B: Environ 2018;225:354–63.

[59] González-Castaño M, Dorneanu B, Arellano-García H. The reverse water gas shift reaction: a process systems engineering perspective. React Chem Eng 2021;6(6): 954–76.

[60] Daza YA, Kuhn JN. CO$_2$ conversion by reverse water gas shift catalysis: comparison of catalysts, mechanisms and their consequences for CO$_2$ conversion to liquid fuels. RSC Adv 2016;6(55):49675–91.

[61] Kim SS, Lee HH, Hong SC. A study on the effect of support's reducibility on the reverse water–gas shift reaction over Pt catalysts. Appl Catal A: General 2012; 423–424:100–7.

[62] Baharoon DA, Rahman HA, Omar WZW, Fadhl SO. Historical development of concentrating solar power technologies to generate clean electricity efficiently—A review. Renew Sustain Energy Rev 2015;41:996–1027.

[63] Blanco M. Advances in concentrating solar thermal research and technology: Woodhead Publishing; 2016.

[64] El-Ehwany AA, Hennes GM, Eid EI, El-Kenany EA. Development of the performance of an alpha-type heat engine by using elbow-bend transposed-fluids heat exchanger as a heater and a cooler. Energ Conver Manage 2011;52(2):1010–9.

[65] Muhich CL, Blaser S, Hoes MC, Steinfeld A. Comparing the solar-to-fuel energy conversion efficiency of ceria and perovskite based thermochemical redox cycles for splitting H$_2$O and CO$_2$. Int J Hydrogen Energy 2018;43(41):18814–31.

[66] Berger RJ, Pérez-Ramırez J, Kapteijn F, Moulijn JA. Catalyst performance testing: Radial and axial dispersion related to dilution in fixed-bed laboratory reactors. Appl Catal A: General 2002;227(1–2):321–33.